THE DEVELOPMENT OF AN ELECTRON GUN FOR PERFORMING ULTRAFAST ELECTRON DIFFRACTION EXPERIMENTS

by

Nicolas Erasmus

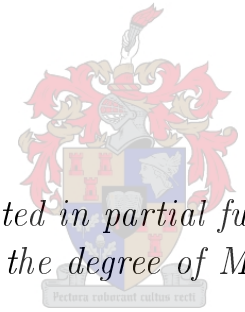

Thesis presented in partial fulfillment of the requirements for the degree of Masters of Science

at

Stellenbosch University

Department of Physics

Faculty of Science

Supervisor: Prof. Heinrich Schwoerer
Co-supervisor: Prof. Erich Rohwer

Date: December 2009

Stellenbosch University http://scholar.sun.ac.za

Declaration

By Submitting this thesis electronically, I declare that the entirety of the work contained therein is my own, original work, that I am the owner of the copyright thereof (unless to the extent explicitly otherwise stated) and that I have not previously in its entirety or in part submitted it for obtaining any qualification.

Date:

Copyright © 2009 Stellenbosch University

All rights reserved

Stellenbosch University http://scholar.sun.ac.za

Abstract

This thesis aims to comprehensively discuss ultrafast electron diffraction and its role in temporally resolving ultrafast dynamics on the molecular level. Theory on electron pulses and electron pulse propagation will be covered, but the main focus will be on the method, equipment and experimental setup required to generate sub-picosecond electron pulses, which are needed to perform time resolved experiments. The design and construction of an electron gun needed to produce the electron pulses will be shown in detail, while preliminary pulse characterization experiments will also be illustrated. An introduction into the theory of electron diffraction patterns and how to interpret these diffraction patterns will conclude the thesis.

Stellenbosch University http://scholar.sun.ac.za

Opsomming

Hierdie tesis het ten doel om ultravinnige elektrondiffraksie deeglik te bespreek asook die rol wat dit speel om ultravinnige tyd-dinamika op ‘n molekulêre vlak op te los. Die teorie van elektonpulse en die voortplanting van elektronpulse sal gedek word, maar die fokus sal op die metode, gereedskap en eksperimentele opstelling wees wat benodig is om sub-pikosekonde elektronpulse te genereer. Die ontwerp en konstruksie van ’n elektrongeweer, wat benodig word om elektronpulse te produseer, sal in detail bespreek word, terwyl aanvanklike pulskarakterisasie eksperimente ook illustreer sal word. ‘n Inleiding tot die teorie van elektrondiffraksie patrone en hoe om hulle te interpreteer sal die tesis afsluit.

Stellenbosch University http://scholar.sun.ac.za

Acknowledgments

Special thanks must go to my laboratory partners, Kerstin Haupt and Günther Kassier, for their contributions in scientific knowledge, simulations, general advice and the positive working environment which they helped create.

For having a relaxed but efficient supervisor like Prof. Heinrich Schwoerer who always has time for discussion or advice I am extremely grateful.

Also a big thank you to all the Laser Research Institute[1] members especially the Kudu-lab physicists and my co-supervisor Prof. Erich Rohwer.

And lastly, none of the experiments would have been possible without all the hardware. So thank you to Mr Botha and Mr Burns from the physics department workshop, Ewald Pietersen from Petgo Engineering and Sparkwell. Sergio Coelho's advice on vacuum systems was also extremely helpful.

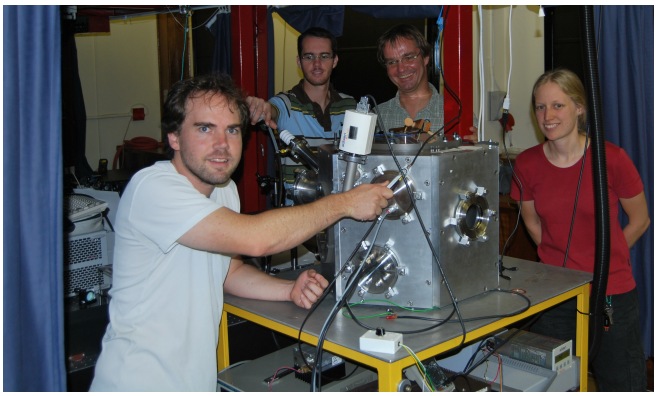

[1] http://www.laser-research.co.za

Stellenbosch University http://scholar.sun.ac.za

Contents

Stellenbosch University http://scholar.sun.ac.za

Stellenbosch University http://scholar.sun.ac.za

List of Figures

Stellenbosch University http://scholar.sun.ac.za

Stellenbosch University http://scholar.sun.ac.za

Stellenbosch University http://scholar.sun.ac.za

List of Tables

Stellenbosch University http://scholar.sun.ac.za

1

Introduction

Ultrafast electron diffraction is a fairly new technique that aims to directly observe the dynamics of solids and molecules on an extremely fast time-scale. This is done by combining two tried-and-trusted techniques, namely: conventional electron diffraction and the 'pump-probe' technique used routinely in ultrafast spectroscopy. The main motivation behind this technique is that it is a more direct and intuitive observation of the molecular dynamics than ultrafast spectroscopy. This is because electrons scatter directly from the entire atomic electrostatic potential, while photons interact with the electron wave-functions. Spatial information of the molecules can therefore be directly derived from the observed diffraction patterns.

Conventional electron diffraction is a well documented field and can be used to observe periodic structures in a solid on the atomic scale (in the Ångström regime i.e. 10^{-10}m) but does not give one time resolved observations. Ultrafast spectroscopy with pulsed laser light on the other hand, enables experimentalists to observe extremely fast dynamics on the atomic scale (in the femtosecond regime i.e 10^{-15}s). The technique however is an indirect observation of the atomic structure, where the dynamics of the molecules are derived from probing electronic energy levels. This is why the combination of the two techniques: conventional electron diffraction and ultrafast spectroscopy, is such an exciting prospect and has already produced some promising results [22, 17] . By generating ultra-short electron pulses, a typical 'pump-probe' setup could be employed to directly observe ultrafast dynamics on the atomic scale.

Another candidate that also meets the necessary requirements for performing ultrafast diffraction experiments would be x-ray pulses. This has been attempted with some success [20], but producing, steering and detecting femtosecond x-ray pulses is not trivial. On the other hand, femtosecond electron pulses are not only fairly simple to produce, but have some other advantages over x-ray pulses as well. Firstly, they are much more inexpensive to produce than x-ray pulses, which either need state-of-the-art, high intensity lasers or bulky, non-tabletop synchrotrons. Secondly, the elastic scattering cross section for an electron is seven orders of magnitude greater [19] than that of a x-ray photon, which means that a much lower flux is needed to produce a useful diffraction pattern. Thirdly, collimating and steering electron beams are far easier. Easily

Stellenbosch University http://scholar.sun.ac.za

built magnetic lenses can be used for focusing and bending magnets used for steering, while steering optics (mirrors and lenses) for x-rays are almost non-existent or extremely inefficient.

Considering all these advantages, femtosecond electron pulses are an excellent and feasible source for producing time-resolved observations of molecular motion on the atomic scale in a typical tertiary institute laboratory. The remainder of this thesis will focus on discussing the design and manufacturing of our electron gun that will be able to produce sub-picosecond electron pulses needed for time-resolved experiments.

Stellenbosch University http://scholar.sun.ac.za

2

How ultrafast electron diffraction works

Conventional electron diffraction has shown us for decades how we can obtain periodic structural information from solids on the atomic scale. To illustrate how this is done a very basic example will be used. If we consider the following diffraction pattern produced by a grating (i.e. large number of equally spaced parallel slits) then we can show that the following equation holds for constructive interference [9]:

$$d \sin \theta = m\lambda, \qquad m = 0, 1, 2, ..., \tag{2.1}$$

where:

- d is the distance between the centers of the slits
- λ is the wavelength
- m is known as the order of the interference fringe, where the first order ($m = 1$) for example is the first fringe on each side of the central fringe

Stellenbosch University http://scholar.sun.ac.za

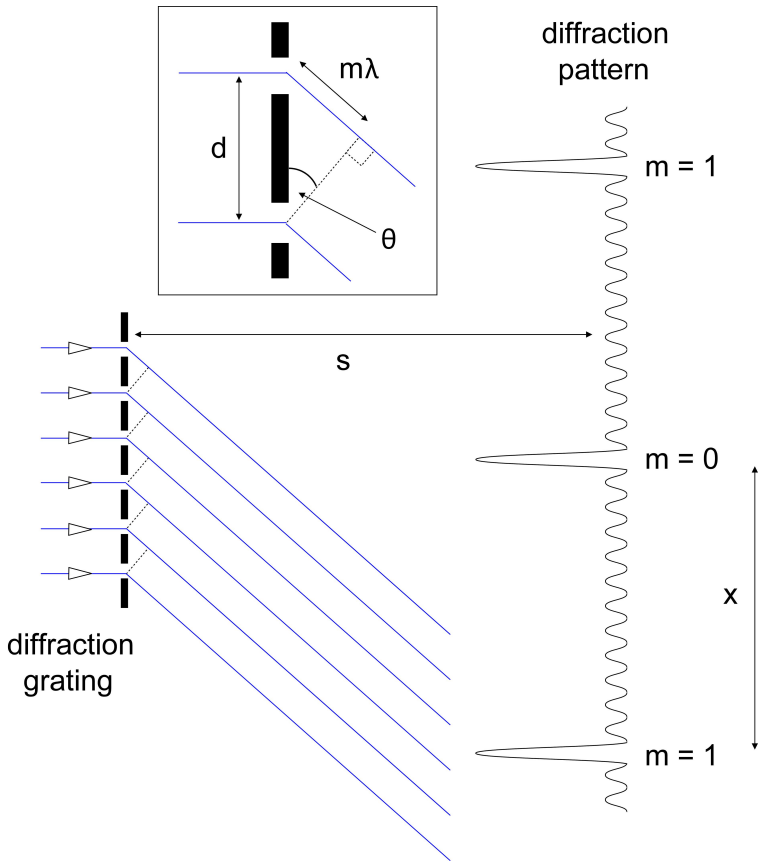

Figure 2.1: Diffraction from a grating.

This is of course an extremely basic example and electron diffraction patterns can be far more intricate. The important idea which is illustrated, is that by measuring angles at which constructive interference occurs we can calculate spatial parameters of the object that produced the diffraction pattern, provided we know the wavelength. In this basic example we would be able to calculate the spacing between the centers of the slits, d, by measuring the distances x and s and calculating the angle θ (d can then be calculated using eq. 2.1 if λ is known). It should also be clear from figure 2.1 and eq. 2.1 that λ should be smaller than d otherwise θ would be to big for constructive interference to be visible on the observation screen. This concept is known as the diffraction limit and is important in the choice of using electrons to produce diffraction patterns from atomic scale periodic structures in solids (see section 3.1).

The following is a typical electron diffraction pattern from a thin ($\sim$ 50nm) metal foil like aluminium or gold. (the difference between polycrystalline and single crystal structure is discussed in chapter 6).

Stellenbosch University http://scholar.sun.ac.za

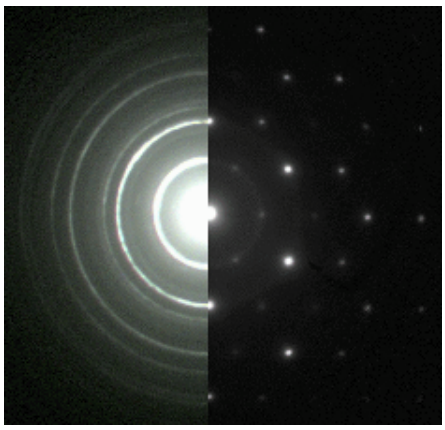

Figure 2.2: Polycrystalline diffraction vs. Single crystal diffraction.

It is then easy to see that by measuring the radii of diffraction rings or the position of diffraction spots, there should be a means of calculating periodic structural information of the sample that produced the diffraction pattern (see chapter 6 for more detail on how these diffraction patterns are formed and analyzed, and which structural parameters can typically be calculated).

Some details involved in electron diffraction have now been discussed, but now the idea should be taken a step further. What would one need to do to observe how these diffraction patterns transform, while the sample undergoes an extremely fast transformation? The duration of photo-induced phase transitions in various materials have been shown to be in the order of a few hundred femtoseconds to a few picoseconds [22, 6, 2]: The solid-to-liquid phase transition of a thin (20nm) aluminium foil upon melting with a laser pulse, has been observed through the transformation of an electron diffraction pattern and was shown to occur in the pico-second regime [22]. The structural transformation in the insulator-to-conductor phase transition of VO_2 has also been observed through the transformation of an electron diffraction pattern and it was shown that some of the processes take place in the order of a few hundred femto-seconds [2]. Insulator-to-conductor phase transitions in organic salts have been observed through ultrafast spectroscopic techniques [6], but it was suggested that x-ray or electron structural analysis on the femtosecond time-scale was needed to clarify the real mechanism of the observed photo-induced phase transition. Detection systems, whether it be a CCD camera or MCP (see chapter 4.6), can simply not operate at such short time scales, since they are limited as all electronic devices are to the nanosecond regime. This is purely because there is a physical limit to the size of their electronic circuits and the speed at which electronic signals can propagate through the circuit. Another technique must therefore be considered.

Fortunately a technique used in ultrafast spectroscopy, known as the 'pump-probe' technique can be applied to this problem. The technique relies on the idea that one converts the time-scale problem to a distance-scale problem (or rather solution). The reason for this is that if we consider the relationship between velocity, distance and time: $v = \frac{d}{t}$ (and the velocity being the speed of

Stellenbosch University http://scholar.sun.ac.za

light), then we see that a few femtoseconds relates to a few microns (1μm $\rightarrow$ 3fs). It was previously mentioned that the detection capabilities of electronic equipment do not fall in the femtosecond regime, but it is however fairly easy to obtain motorized translation stages that function in the micrometer regime. By using this to our advantage we can, with some effort, detect in the femtosecond regime with a so called 'slow' detector.

The basic idea behind the 'pump-probe' technique is the following (see fig 2.3)[1]: A change is induced in the sample by means of a 'pump' pulse at time zero, while the change by means of a 'probe' pulse at a later time, t, is observed. A so called 'slow' detector can be used to detect the signal induced by the 'probe' pulse, since all signal collected by detector over a period of time can only reveal the state of the sample at the time, t, after the 'pump' pulse arrived at the sample. In our case the 'pump' pulse would typically be a light pulse (assuming we want to observe a photo-induced transformation) and the probe pulse would be an electron pulse (which will produce our diffraction pattern). Repeating the experiment and varying the time, t, by increasing/decreasing the optical path length of one of the pulses, the motion of the atoms or molecules in the sample as it undergoes its transformation can be observed. The time resolution between one observation and the next is then simply determined by the resolution at which one can increase/decrease the path length and of course the pulse duration.

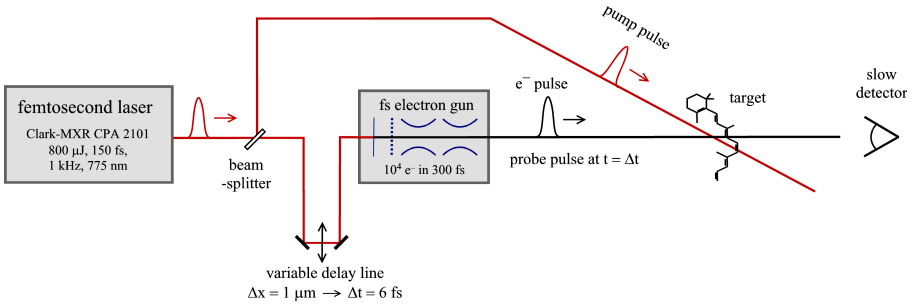

Figure 2.3: Typical pump-probe setup with a photo-induced change in the sample triggered by an optical 'pump' pulse and the change observed by an electron 'probe' pulse.

[1] In the sketch it is indicated that 1 μm $\rightarrow$ 6 fs and not 3 fs like previously stated. This is because by increasing the translation stage by 1 μm the pulse travels an extra 2 μm and therefore has a 6 fs time difference.

Stellenbosch University http://scholar.sun.ac.za

3

Short electron pulses

3.1 Wave-particle duality of electrons

When electrons are spatially confined, for example when they are being forced to propagate through a double slit, they behave in a wave-like manner. The requirement is that the scale of the confinement (i.e. slit width and slit separation) should be comparable to an electron's de Broglie wavelength, $\lambda = \frac{h}{p}$ (with $h = 6.63 \times 10^{-34}$ J·s and p its momentum). This wave-like behavior makes it possible for them to produce diffraction patterns.

In order for the electrons to produce diffraction patterns from crystal lattices, the wavelength has to be on the order of the lattice spacing of a crystal, in other words a few Ångström (see chapter 2). For non-relativistic electrons ($v << c$ or $E_k << 500$ keV), the wavelength of an electron can be expressed in terms of its kinetic energy, $E_k = \frac{1}{2} m_e v^2$, as

$$\lambda = \frac{h}{\sqrt{2 m_e E_k}} \tag{3.1}$$

with $m_e = 9.11 \times 10^{-31}$ kg, the rest mass of an electron [9]. The following figure shows the wavelength of an electron as a function of its kinetic energy.

Stellenbosch University http://scholar.sun.ac.za

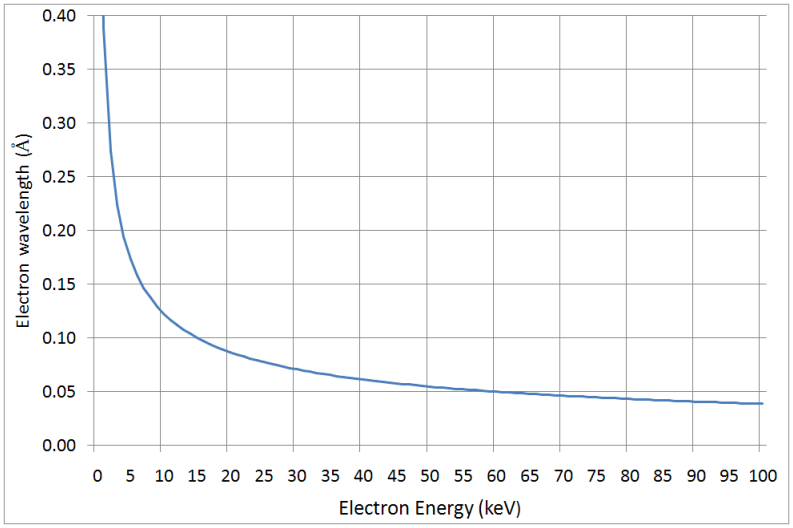

Figure 3.1: Electron wavelength as a function of kinetic energy.

From fig 3.1 we can see that the de Broglie wavelength of an electron with a kinetic energy between 1 keV and 100 keV (i.e. non-relativistic) ranges roughly between 0.4 - 0.04 Å. Non-relativistic electrons in this energy range therefore satisfy the diffraction limit if one wants to observe atomic structure through diffraction patterns.

The only remaining criteria needed for time-resolved experiments is to produce electron pulses in the femtosecond regime. The remainder of this chapter explains why this is necessary and how it can be done.

3.2 Why short pulses are needed

The time resolution between one observation and the next in a 'pump-probe' setup (see figure 2.3) is determined by the resolution of the translation stage and duration of the pulses.

Let us consider the following analogy to explain the concept: We want to video record a man running the 100 meters (from point A to point B) in 10 seconds. We assume that the video consists of a collection of images, where the exposure time of each image is $\triangle t$. The total time of the event is t, in this case 10 seconds. We also have another variable $\triangle \tau$, which represents the time between when image n and image $n+1$ is taken. See fig. 3.2 for more clarity.

Stellenbosch University http://scholar.sun.ac.za

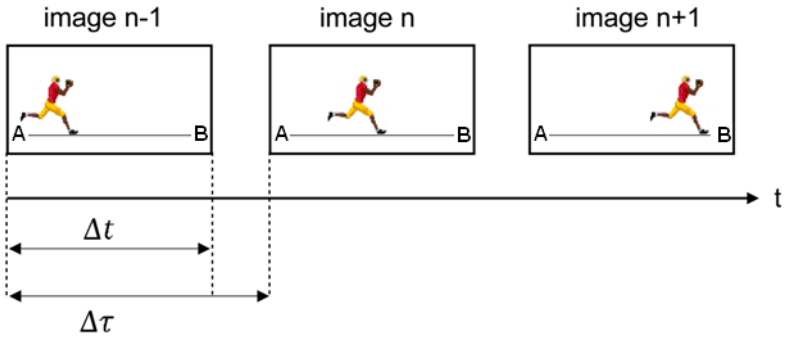

Figure 3.2: Running man analogy for the observation method in a 'pump-probe' experiment.

In this analogy the the man represents the molecule that is being observed where at position A the molecule is in its initial state and at position B it is in its final state (due to the pump pulse). The time interval $\triangle t$ represents the probe pulse duration and $\triangle \tau$ the time resolution determined by the translation stage. The 'clap' of the starting-gun represents the 'pump-pulse' and this triggers the event (the start of the race in this case). Sticking with the analogy we can see that in order to make a smooth video, $\triangle \tau$ should ideally be the same length as $\triangle t$[1] such that the image $n+1$ takes over where image n left off. Also $\triangle t$, the exposure time, has to be shorter than the total duration of the event, t, otherwise the whole event will be smeared out over one image. To make a sensible video many images are required, and therefore $\triangle t$ should be a fraction of the total time t.

This analogy is of course not completely compatible with the 'pump-probe' technique unless one assumes that only one image can be taken during the entire event. If the entire event needs to be recorded by taking say 10 images, one would have to repeat the event 10 times. For each repetition of the event the time at which the image is taken should increase in multiples of $\triangle \tau$. The assumption that the man runs the 100 m in an identical fashion every time also has to be made.

It should however be clear from this analogy that if one wishes to observe ultrafast atomic motion (in the pico-to-femtosecond regime) by means of a 'pump-probe' setup, electron pulses in the femtosecond regime would need to be produced.

3.3 Electron pulse generation

The photo-electric effect and thermionic emission (heating of a metal) are two methods to generate free electrons. For reasons that will become apparent at

[1] In a 'pump-probe' experiment $\triangle \tau$ is often smaller than $\triangle t$ to have some overlapping of observations.

Stellenbosch University http://scholar.sun.ac.za

the end of this section, the photo-electric effect is chosen as the method for generating electron pulses. The photo-electric effect refers to the phenomenon that light has the ability to emit electrons out of the surface of a material. Einstein's theory [10] explains that when the photon interacts with the material, its energy is transferred to the material and contributes to the energy needed to emit an electron. Since electrons are held in the material by attractive forces, there is a minimum photon energy needed to emit the electron from the material. This minimum energy is known as the work function and is different for different materials. The work function is relevant when referring to atoms inside a solid and should not be confused with the ionization energy, which is defined as the energy needed to remove an electron from a single 'free-standing' atom. The energy of a photon is $E = h\nu = \frac{hc}{\lambda}$ with $c = 3\times10^8$ m/s, the speed of light in a vacuum.

The work function for a thin ($\sim$ 150 nm) gold foil, a metal often used in electron guns, has been experimentally measured to be 5.10 eV or 8.17×10^{-19} J [16]. The value for the work function is not a fixed value because it is strongly dependent on the surface quality of the foil. The work function is also dependent on the thickness and crystalline orientation of the material and therefore the value of the work function can easily vary by $10 - 15$ %. There are also two types of methods used to calculate the work function namely: absolute and relative, and there is an ongoing debate over which is more accurate. In the absolute method, the kinetic energy of the emitted electron is measured as a function of the input energy. The input energy can take the form of photon-energy (photo-emission), temperature increase (thermionic emission) or an electric field (field electron emission). The work function is then given by the difference between the input energy and the electron's kinetic energy, $W = E_k - E_{in}$. In the relative method, the contact potential difference between the sample and a reference electrode is measured.

Using the experimentally measured work function for a 150 nm thick gold foil, the maximum wavelength of light needed for emitting electrons can be calculated:

$$\lambda = \frac{6.63 \times 10^{-34}\ \text{J}\cdot\text{s} \times 3 \times 10^8\ \text{m/s}}{8.17 \times 10^{-19}\ \text{J}} = 2.55 \times 10^{-7}\ \text{m} = 241\ \text{nm}.$$

The result shows that in order to emit electrons from gold we need to illuminate it with UV light.

Below is a table of commonly used metals and the corresponding wavelength needed to emit electrons [16, 8]:

Metal (~150 nm thick)	Work Function (eV)	Ionization Energy (eV)	Maximum Wavelength (nm)
Gold (Au)	5.10	9.23	241
Silver (Ag)	4.26	7.58	289
Aluminium (Al)	4.28	5.98	288

Table 3.1: Work functions of common metals.

Stellenbosch University http://scholar.sun.ac.za

A typical setup (see fig 3.3) for electron generation entails illuminating a thin ($\sim$ 20 nm) metal coating with laser light at the required wavelength. In this setup the metal coating is deposited on a clear window in such a way that the coating can be illuminated from the rear. This is not necessary but is the geometry used in the design of our electron gun. The kinetic energy of the emitted electron is given by the difference between the photon energy and the work function of the metal, $E_k = h\nu - W$. This is typically less than 1 eV, not near the $1 - 100$ keV needed as discussed in section 3.1. A strong electric field is therefore introduced to accelerate the electrons to the required kinetic energy and in the desired direction.

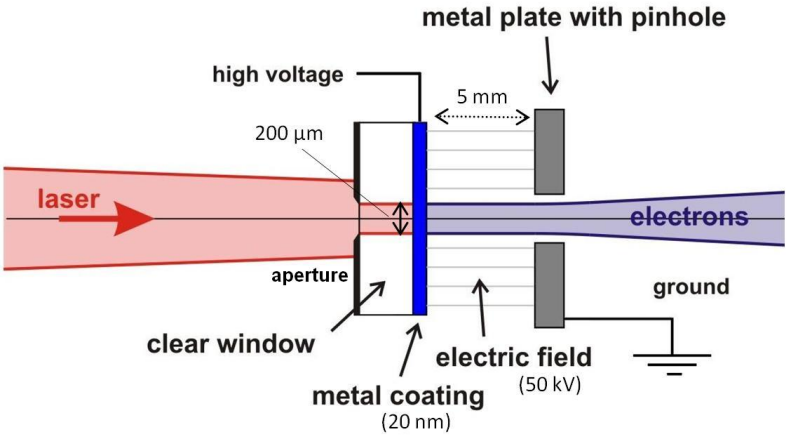

Figure 3.3: Typical setup for electron production.

In order to produce short (a few hundred femtoseconds) electron pulses, one can simply exchange the light source employed for the photo-electric effect by a femtosecond pulsed laser. Since electrons are only emitted when there are photons present, electrons are only emitted during the duration of the laser pulse. The electron pulse will therefore have the same temporal duration and spatial profile as the laser pulse at the point of generation [19].

3.4 Electron pulse propagation

The following figure shows the propagation schematic of the electron pulse, from generation to interaction with the sample, in a typical ultrafast electron diffraction setup (see also figure 3.3).

Stellenbosch University http://scholar.sun.ac.za

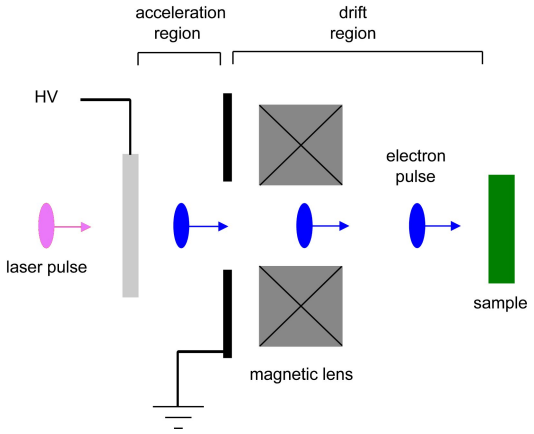

Figure 3.4: Electron propagation from generation to sample interaction.

The biggest challenge in ultrafast electron diffraction experiments is to produce sub-picosecond pulses with sufficient electron densities (at least 10^4 electrons/pulse). The high electron densities are needed for the diffraction patterns to have a usable image resolution, but on the other hand space charge effects (Coulomb repulsion) and the initial kinetic energy distribution of the electron pulse at these densities broaden the electron pulse duration significantly as it propagates. It has been shown that pulse duration broadening due to initial kinetic energy distribution can be minimized by accelerating the electrons as fast as possible (i.e. have the extracting electric field as large as possible). The radial spread of electrons can also be counteracted by means of a magnetic lens. The space charge effect however is still problematic in the drift region and the solution is usually to shorten the propagation distance to the sample as much as possible. Space charge effects also have a broadening effect on the kinetic energy distribution, which has the potential to influence the diffraction pattern. It is therefore clear that the propagation dynamics have to be fully understood when designing an ultrafast electron gun.

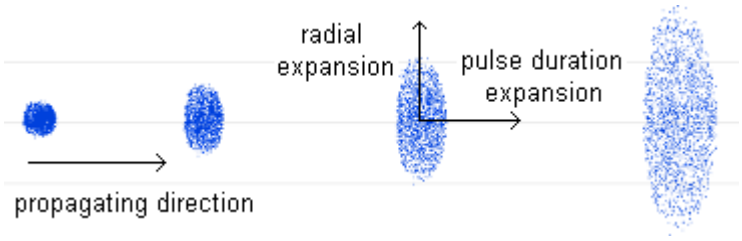

Figure 3.5: Graphical depiction of electron bunch expansion as it propagates.

In an attempt to understand the propagation dynamic of electron pulses two methods have been used, namely: N-body simulations and the mean-field model. It has been shown that these two methods have an excellent agreement when showing and predicting the propagation dynamics of an electron pulse in the drift region [21]. The acceleration distance is only about $3-5$ mm (acceleration

Stellenbosch University http://scholar.sun.ac.za

voltage 30−50 kV), therefore the electrons spend much less time (roughly 50 ps) in this region than in the drift region, which can be a few centimeters (velocity of a 30 keV electron is roughly $\frac{1}{3}c$, i.e. 10 cm/ns). The drift region is therefore the biggest contributor to pulse duration broadening. Using N-body simulations and the mean-field model, the propagation over 40 cm of a Gaussian femtosecond electron pulse was simulated by Siwick et al. [21] ($N = 10000$ electrons, $\tau_0 = 90$ fs, $r(0) = 250$ μm and $E_k = 30$ keV, $\triangle E_k(0) = 0.6$ eV). It was shown that electron pulse duration has an initial quadratic propagation time dependence (over the first $10 - 15$ cm) and thereafter the pulse duration increases linearly with time. The pulse duration was close to 500 fs at 10 cm propagation distance and almost 5 ps at 40 cm propagation distance. The kinetic energy distribution was shown to increase rapidly and then approach a constant at long propagation distances. The kinetic energy distribution was close to 40 eV at 10 cm propagation distance and almost reached a constant of 100 eV at 40 cm propagation distance. It was also shown that the induced kinetic energy distribution resulted in the development of a linear velocity chirp on the electron pulse and it was suggested that this could be used for possible pulse recompression. It should therefore be clear that the propagation dynamics of an electron pulse should be clearly understood when designing and incorporating an electron gun into an ultrafast electron diffraction experimental setup.

Simulations by Kassier et al. [15], a member of our research group, has shown that with some effort one can construct a reflectron to counteract pulse duration broadening due to space-charge effects by recompression of the electron pulse. It was shown that a 100 keV electron pulse with 200000 electrons was recompressed to a pulse duration of only a 130 fs. Static electron optics such as electric fields and magnetic lenses are used to recompress the chirped electron pulse. The main component used to compress the pulse again is a static electric field similar to the one used for accelerating the electrons (see figure 3.3). The Coulomb repulsion within the electron bunch, produces a linearly chirped pulse, implying that the electrons at the front of the pulse have a higher kinetic energy (i.e. higher velocity) than those at the rear of the pulse. These 'faster' electrons penetrate deeper into the electric field and therefore follow a longer path than the 'slower' electrons at the rear of the pulse. This difference in path-length results in a recompressed pulse.

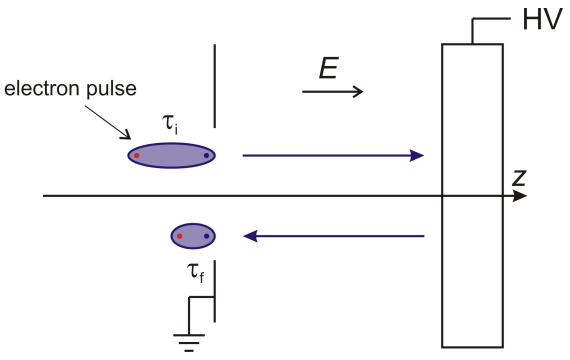

Figure 3.6: Principle of recompression in a reflectron - the front, 'faster' electrons penetrate deeper and hence have a longer path length.

Stellenbosch University http://scholar.sun.ac.za

The previous sketch shows the reflection taking place parallel to the propagating direction. This is entirely unpractical since it would then be impossible to place a sample in the beam-path of the compressed pulse without blocking the uncompressed pulse from entering the reflectron. To overcome this obstacle one could typically send the uncompressed pulse into the reflectron at a slight angle. Other difficulties, such as induced pulse tilting, then become a factor but it was shown that this can theoretically be compensated for by a pair of bending magnets [15].

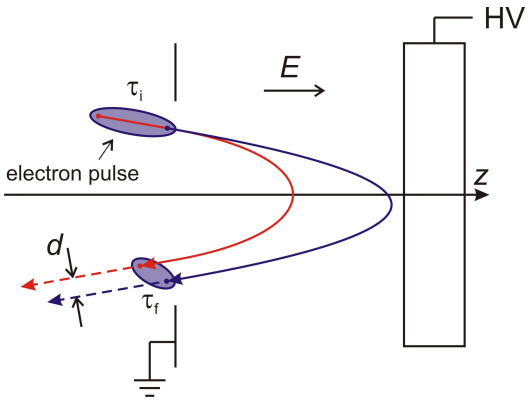

Figure 3.7: A more practical reflectron with the electron pulse entering the reflectron at an angle.

The next chapter will discuss how our electron gun was designed and manufactured based on the discussion of this chapter. It will also be shown how the electron gun was incorporated into an experimental setup to produce sub-picosecond electron pulses in order to perform time resolved electron diffraction experiments.

Stellenbosch University http://scholar.sun.ac.za

4

Experimental setup

The ultrafast electron diffraction group at the Laser Research Institute was established in 2007 with two PhD. students, Günther Kassier and Kerstin Haupt. Preliminary work predominantly focused on electron pulse propagation simulations and electric field simulations for the electron gun, and in February 2008 I joined the group as a MSc. student. We worked together closely to set up the experiment but each individual was allocated specific tasks. My tasks included, but were not limited to, the final design of the electron gun, setting up the vacuum system and detecting our first electron diffraction pattern. In the same way the other students were not limited to their tasks and therefore I also received a lot of input and help from the two PhD students and my supervisor with my tasks. As this is the first thesis written on the progress of the ultrafast electron group, I will give an overview of the entire experimental setup since different component can not be viewed separately from the entire project but I remind the reader that not all the work was done by myself.

The experimental setup consists of six main components: 1) the femtosecond laser; 2) the UV light generation; 3) the electron gun; 4) the magnetic lens; 5) the vacuum chamber with vacuum pumps and 6) the electron detection. The topography of the experimental setup is shown in the following figure:

Stellenbosch University http://scholar.sun.ac.za

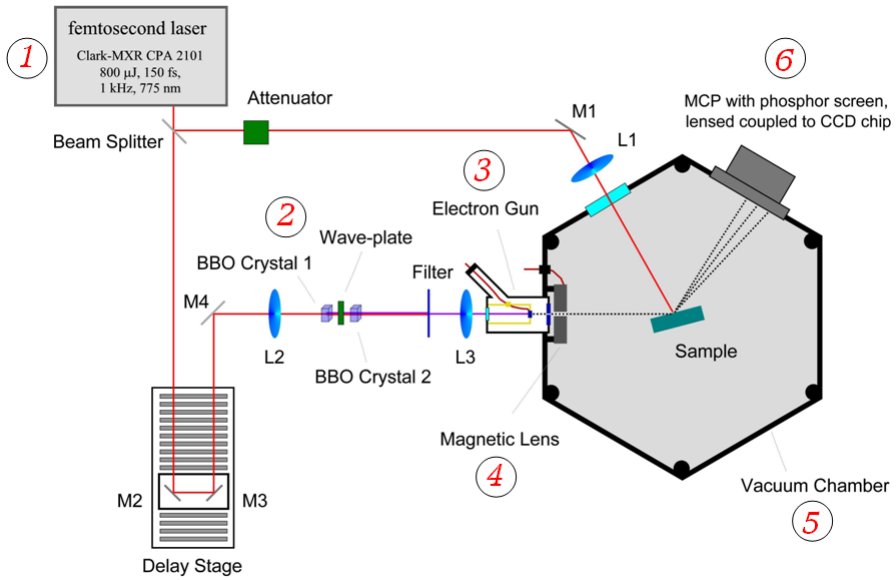

Figure 4.1: Experimental setup.

The six main components labeled on the experimental setup will now be discussed in detail.

4.1 The femtosecond laser

The laboratory is equipped with a Clark MXR 2101 laser. The laser employs a chirped pulse regenerative amplifier, which has a Ti:Sapphire crystal pumped with a 10 watt (operated at $\sim$ 7 watt), Nd:YAG laser at 532 nm (frequency doubled from 1064 nm). The seed pulse for the amplifier is supplied by an Erbium doped fiber ring laser which produces 775 nm pulses, frequency double from 1550nm. The Clark laser ultimately produces $\sim$ 800 μJ pulses with a duration of roughly 150 fs. The wavelength of the pulses are 775 nm with a repetition rate of 1 kHz. The laser is a complete 'turn-key' device and does not require any alignment on a daily basis.

4.2 UV light generation

The UV laser light needed to generate the electrons is produced by a two-stage frequency tripling of the fundamental light (775 nm). The light is first frequency doubled to 388 nm by the first BBO crystal and then the remainder of the fundamental is frequency summed with the 388 nm in the second BBO crystal to produce the UV (258 nm) light. In section 3.3 it was calculated that light with wavelength of 241 nm is needed for generating free electrons from a $\sim$ 150 nm gold foil but can vary by $10-15$ % depending on the surface quality and thickness of the foil (our gold coating is $\sim$ 20 nm). The UV spectrum generated has bandwidth of $\sim$ 2 nm. The third harmonic of the fundamental should therefore be sufficient to generate electrons.

Stellenbosch University http://scholar.sun.ac.za

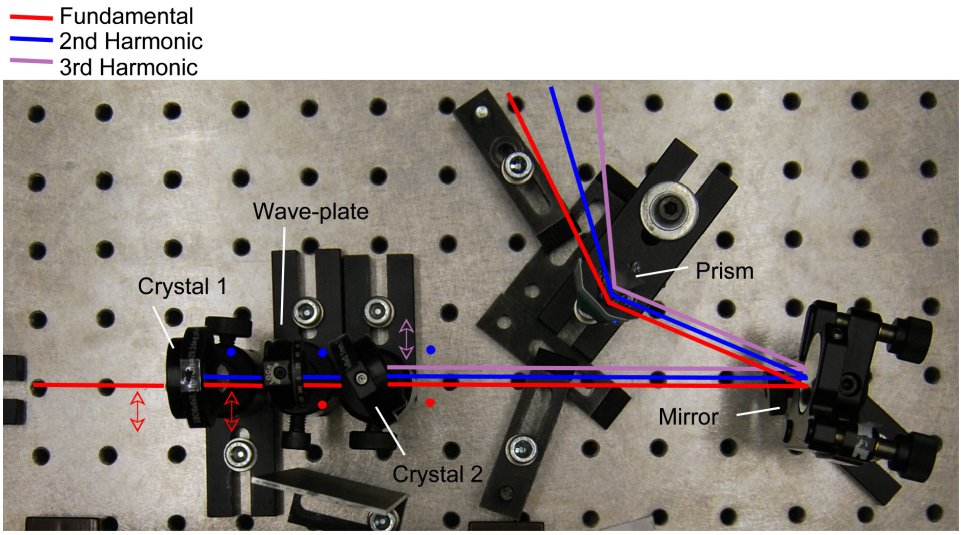

Figure 4.2: UV light setup.

Type 1 phase matching is used in both crystals. This implies that both incoming wavelengths have to be ordinary polarized with respect to the optical axis of the crystal and that the generated wavelength is extraordinary polarized with respect to the optical axis. This required a half-waveplate (for 775 nm) to be placed between the two crystals, which rotated the remainder of the fundamental by 90 degrees and the second harmonic by 180 degrees (see fig 4.2, the dot indicates polarization out of the page and the arrow indicates polarization in the plane of the page). This ensures that the polarization is the same when they enter the second crystal. Both crystals are cut at 30 degrees which is the required angle for the frequency doubling of 775 nm light. The angle required for frequency tripling in the second crystal is 58 degrees which explains the ~ 28 degree orientation of the second crystal (see fig 4.2).

A 500 mm focal length lens is used to provide enough intensity for the nonlinear processes inside the crystals but still maintain a fairly long Rayleigh length. This allows both crystals to be in close vicinity of the focus. The third harmonic is separated from the fundamental and second harmonic light by dispersing it through a MgF prism. The average power of the UV (third harmonic) light can be adjusted between about 1 μW and 80 μW by varying the input of the fundamental between about 1 mW and 30 mW. Fine tuning of the UV power can be done by rotating the wave-plate (this reduces the efficiency of the third harmonic generation).

The following figure shows the spectrum and bandwidth of the generated UV light.

Stellenbosch University http://scholar.sun.ac.za

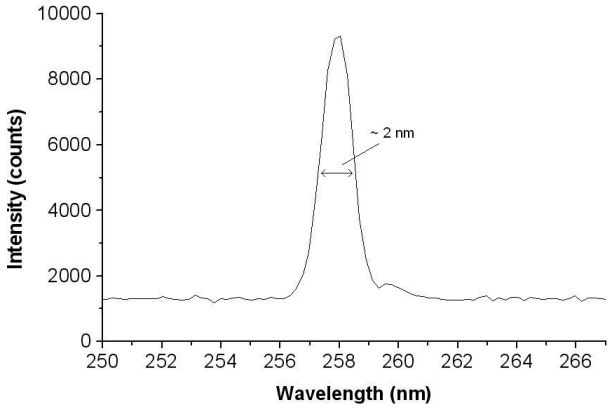

Figure 4.3: Spectrum of generated UV light.

4.3 Electron gun

In chapter 3.3 the basic idea of how electron pulses are generated was explained, but there are some practical limitations that have to be considered when designing an apparatus that can perform the necessary task. Such apparatuses have been successfully designed and manufactured in the past [23, 7, 14] and are commonly referred to as ultrafast electron guns. The origin of the name stems both from its purpose and from its external appearance. The design of our ultrafast electron gun was based on the successful designs of Siwick et al. [23] and Dwyer et al. [7].

The three most important challenges when designing such a gun are: keeping the acceleration distance as short as possible (discussed in chapter 3.4), getting the sample as close to the electron source as possible (discussed in chapter 3.4) and preventing charge breakdown when working with high voltages ($30-50$ kV). The high voltage is needed for the strong extraction field shown in fig. 3.3.

In the sub sections that follow, the important parts or building-blocks that make up our designed and manufactured electron gun will be discussed. Our proposed gun design[1] is shown in fig 4.4 and 4.5 and was built by Petgo Engineering in Cape Town from these designs. The idea is that the pulsed laser beam would enter the gun from the rear through the quartz window, travel through the center of the macor tube and illuminate the metal coated window (cathode) from behind (see fig 3.3). Electrons would then be produced on the front surface of the cathode and be extracted from the gun, through the pinhole in the anode, by a strong electric field between the cathode and anode. Note that the outer shell of the electron gun, as seen in the second figure, does not consist of glass as it appears but was rendered with this texture to make the interior of the gun visible. The outer shell consists of high grade stainless steel as do all the gray components on the 3D rendering of the gun.

[1] Design done in *Autodesk Inventor 2008*

Stellenbosch University http://scholar.sun.ac.za

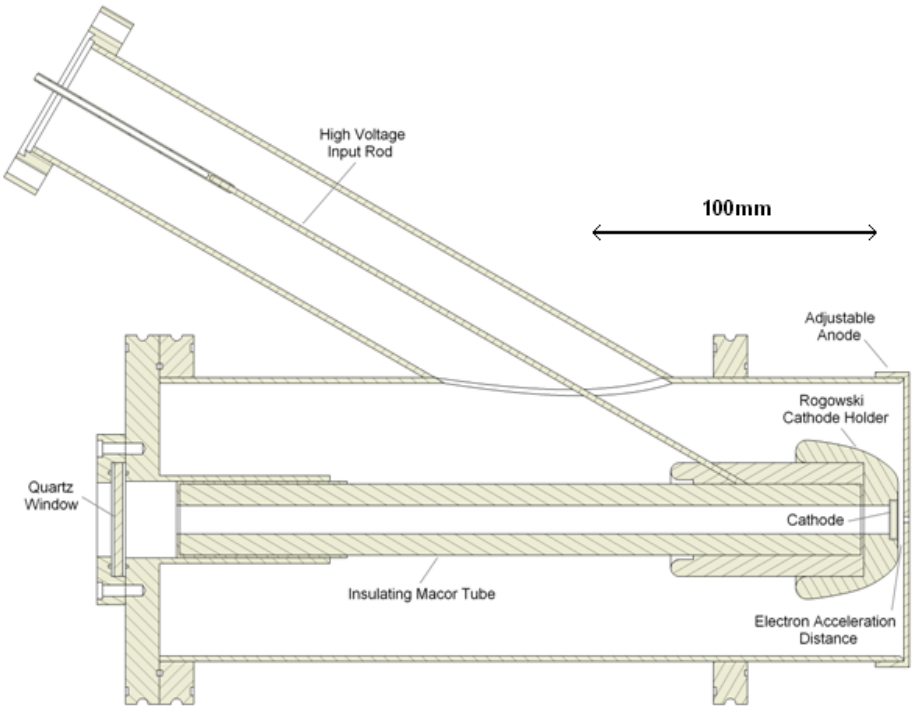

Figure 4.4: Cross-sectional view of electron gun design.

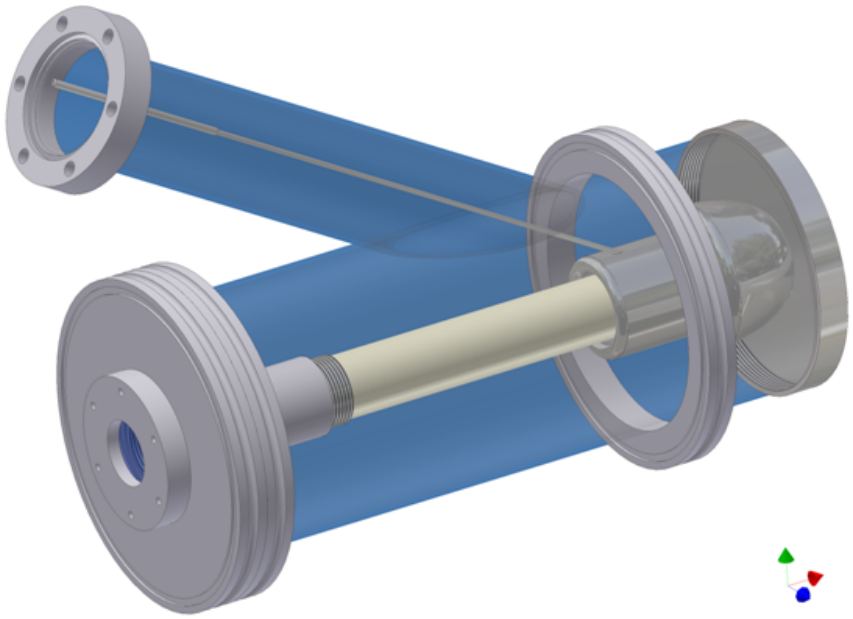

Figure 4.5: Three dimensional rendering of assembled electron gun design.

Stellenbosch University http://scholar.sun.ac.za

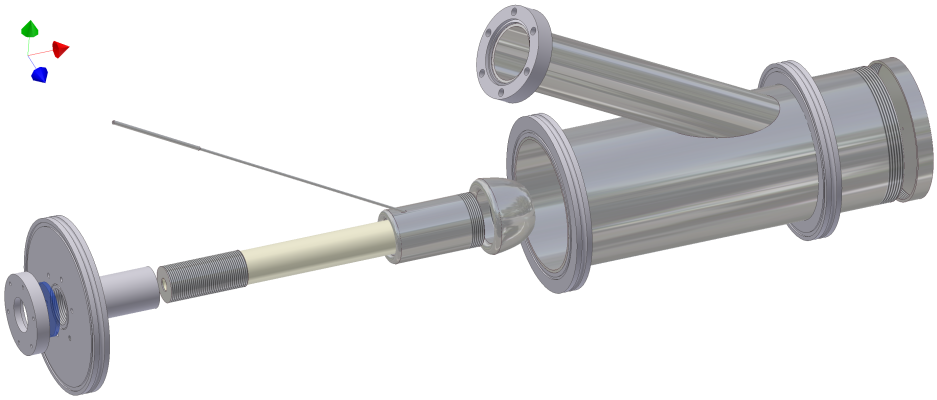

Figure 4.6: Three dimensional rendering of disassembled electron gun design.

4.3.1 Acceleration distance

The strong electric field needed to accelerate the electrons to the required kinetic energy (see chapter 3.1) is created by placing a strong potential across the cathode window and anode cap (see fig 4.4). This is done by placing a high voltage ($30 - 50$ kV) on the cathode and grounding the anode cap (see fig 3.3). It is also important that the electric field is uniform in this area such that all the electrons experience the same accelerating force. This preserves the geometry of the pulse and therefore maintains the minimum time resolution possible in the 'pump-probe' experiment. If the electric field was stronger on one side of the gap, then the pulse would appear skew since the electrons in the stronger electric field would be accelerated faster. This would typically happen when the surface of the cathode and the surface of the anode are not parallel to one another.

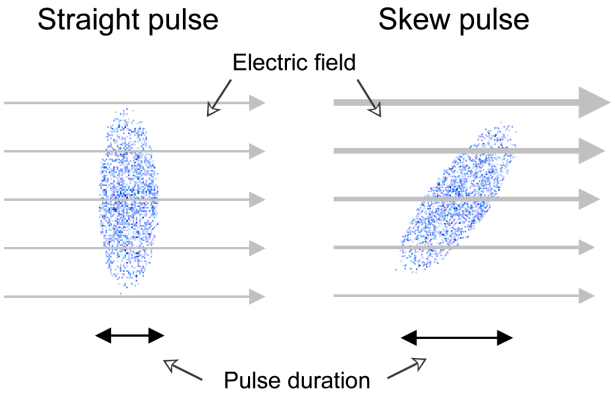

Figure 4.7: Uniform vs. Non-uniform electric field.

In chapter 3.4 it was mentioned that accelerating the electrons as fast as possible (i.e. minimize the accelerating distance and maximize the potential) should minimize the electron pulse duration broadening due to initial kinetic energy distribution. This means that the anode and cathode have to be as close as

Stellenbosch University http://scholar.sun.ac.za

possible to each other. In order to avoid electric discharge between the anode and cathode some simulations[2] were done with various geometrical setups to obtain the desired design specifications. Staying clear of any sharp edges when considering a design is recommended, since electrical discharge occurs easiest at these points. It was found that by embedding the cathode window in a Rogowski profiled head, we could make the gap as small as possible and still minimize the chance of electrical discharge (which would destroy the accelerating electric field or destroy the cathode coating). The Rogowski profiled holder provided a secure and stable location for the cathode window and had the perfect geometry for producing a uniform electric field between the cathode and anode cap (see figure 4.9 for simulated electric field). The desired design specification was set at 100 kV/cm.

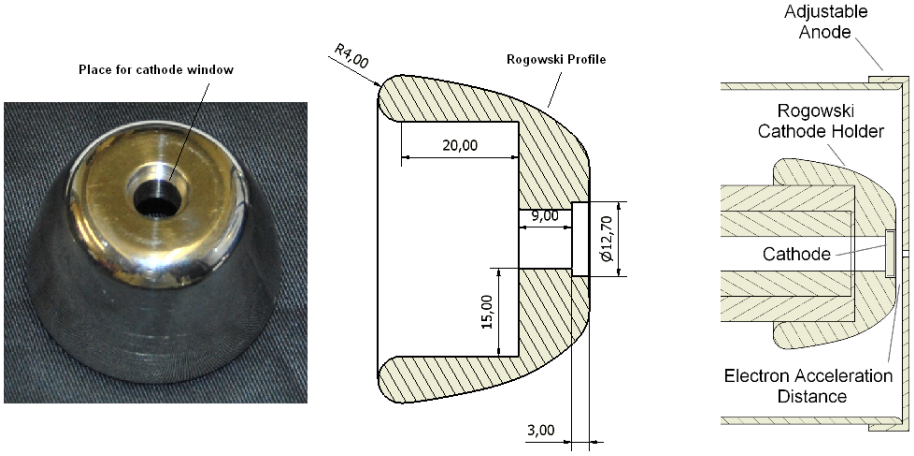

Figure 4.8: Machined Rogowski profiled cathode holder, dimensions and incorporation in electron gun.

[2]Simulations thanks to PhD student Kerstin Haupt. The cathode holder was over-designed for 60 kV with a 3 mm gap, even though one would typically run the electron gun at about 30 kV with a 3 mm gap.

Stellenbosch University http://scholar.sun.ac.za

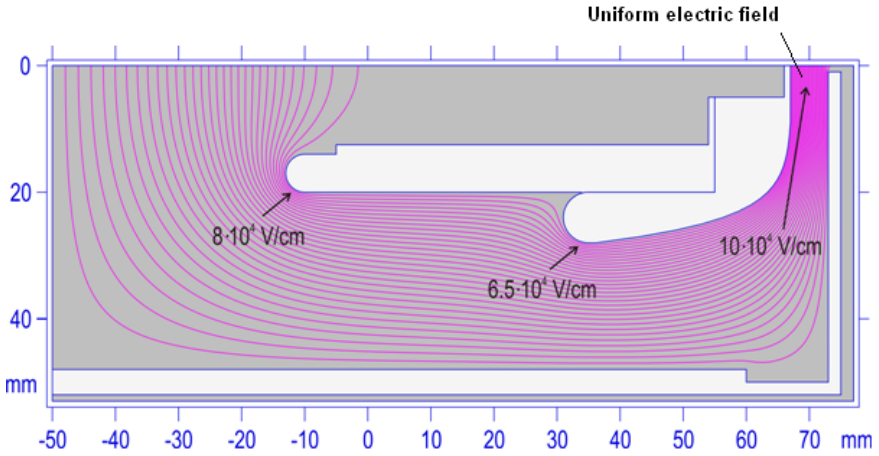

Figure 4.9: Simulation of expected electric field with Rogowski profiled cathode holder (60 kV, 6 mm gap).

4.3.2 Cathode Window

The major considerations when selecting a metal to coat the cathode window with are the work function of the metal and the available laser wavelength. The most common metals used usually have a work function that falls in the UV range ($200-300$ nm) (see table 3.3). The laser in the laboratory produces laser light with a wavelength of 775 nm (see section 4.1). It was therefore decided to use the third harmonic of the CPA (258 nm) and coat the cathode with gold, which has an experimental work function of 5.1 eV $\pm$ 15% (see chapter 3.3). This translates to a required wavelength of 241 nm $\pm$ 35 nm. The metal coating should also be very thin (roughly 20 nm) but still be able to make good electrical contact with the Rogowski profiled head (the high voltage is connected to the Rogowski head and not the cathode window itself). It was decided to coat the window with a thicker layer on the sides and edges to guarantee electrical contact and only have the thin layer in the center of the window[3]. The cathode window is secured in place by coating the sides with electrical silver paint which acts as an adhesive and ensures electrical contact.

[3]Coating thanks to Sergio Coelho from the University of Pretoria, Physics Department.

Stellenbosch University http://scholar.sun.ac.za

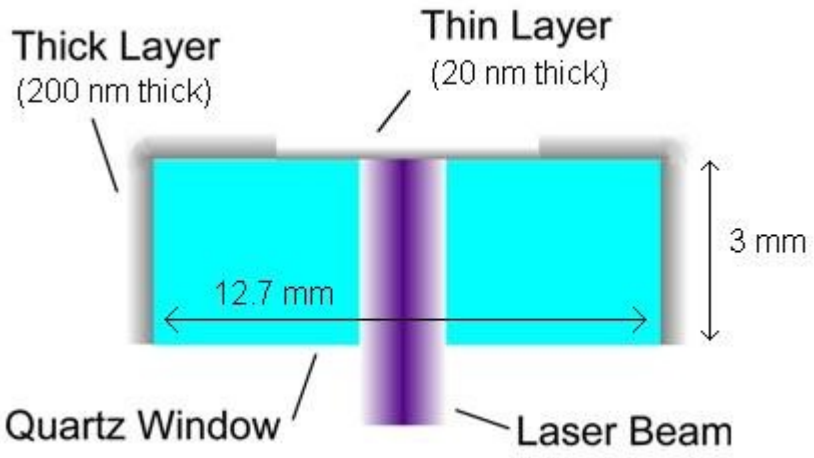

Figure 4.10: Cross-sectional view of gold coating on cathode window - thicker layer on the sides and around the corners for better electrical contact with Rogowski holder.

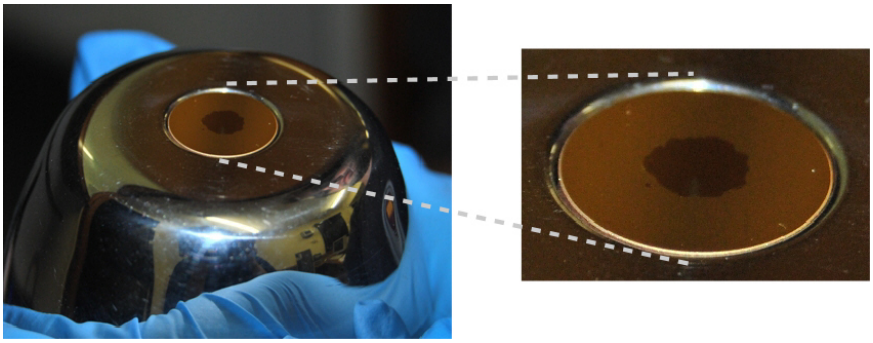

Figure 4.11: Cathode window embedded in Rogowski profiled holder - the central, thinner layer is clearly visible as a darker region.

4.3.3 High voltage connection and insulating macor

The high voltage needed for the extracting electric field brings new challenges to the forefront. The cathode needs to be insulated from the rest of the gun, which is grounded, the laser beam needs to illuminate the cathode from the rear, the acceleration distance needs to be adjustable and the gun needs to be easily assembled and disassembled. This becomes rather tricky when practical, physical and manufacturing limitations have to be taken into account. Many geometries were considered but at the end of the day a design seen in fig 4.4 was agreed upon. The idea is that a macor[4] tube is used the suspend the cathode in free space and therefore insulate it from the rest of the gun. The macor has a hollow core which allows the laser beam to travel down the center and

[4]Macor is a machine-able glass-ceramic. It has excellent thermal characteristics, good electrical insulation and produces very little out-gassing.

Stellenbosch University http://scholar.sun.ac.za

illuminate the cathode from the rear. Both ends of the macor tube have stainless steel threaded caps glued on, the front one thicker to allow for the high voltage rod connection. The threads on each serve different purposes. The thread on the rear cap serves as a way to secure the macor tube to the rest of the gun as well as a means to adjust the acceleration distance. The thread on the front cap makes it possible to secure the Rogowski head onto the tube.

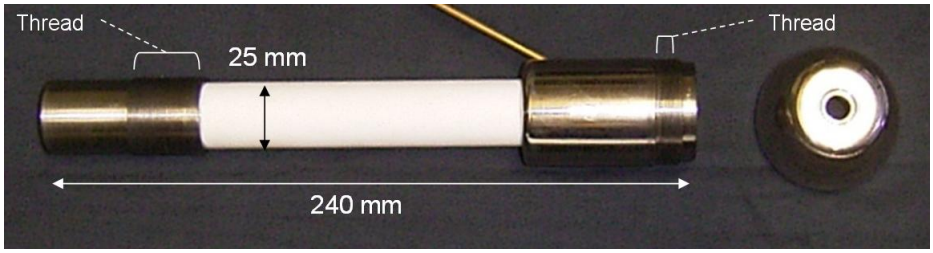

Figure 4.12: Macor tube with glued threaded end caps and Rogowski head.

The high voltage is then connected to by means of a copper rod which screws into the front macor cap. A high voltage, vacuum feed-through is then used complete the connection by sliding into the sleeve attached to the other end of the copper rod.

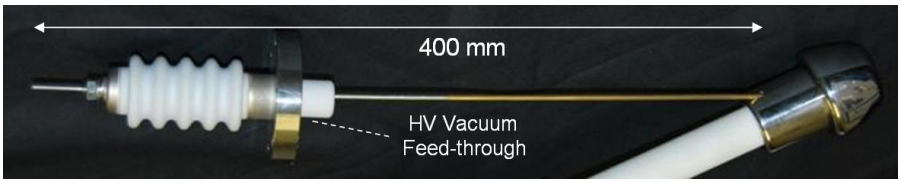

Figure 4.13: High voltage vacuum feed-through.

4.3.4 Gun shell, rear window flange and anode cap.

All the components are then kept in place by means of the outer gun shell shown below. The laser beam can enter the gun through the quartz window (quartz is needed for UV transmission) which is mounted on the rear flange of the gun.

Stellenbosch University http://scholar.sun.ac.za

Figure 4.14: Outer shell of electron gun and rear quartz window flange.

The final component of the gun is the anode cap which has a 2 mm hole in the center through which the electrons exit the gun. Originally the anode cap was designed in such a way that the cap secured onto the gun by means of a thread which could also be used to fine adjust the acceleration distance. However, this was abandoned since guaranteeing a perfectly round thread after welding components onto the gun was nearly impossible. The cap is therefore secured onto the gun by means of 4 'grub' screws which can bee seen in fig 4.15. To ensure no electrical discharge occurred between the cathode window and anode cap the inside of the anode cap was polished to a mirror-like finish. After polishing we could achieve a 50 kV potential across the cathode window and anode cap, with a 5 mm gap (i.e 100 kV/cm electric field strength), without any electrical discharge taking place. This was the desired design specification of the electron gun.

Stellenbosch University http://scholar.sun.ac.za

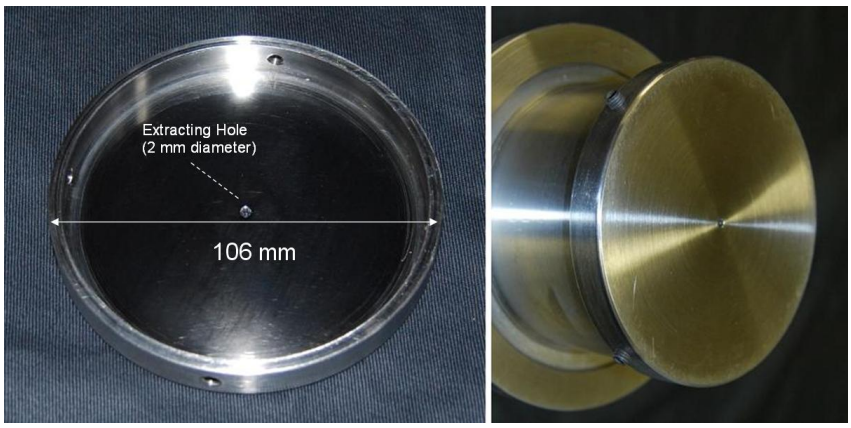

Figure 4.15: View of anode cap's polished inside surface, and cap secured to front of the gun.

4.3.5 Completed gun and Installation

The gun is easily assembled in five steps. Please see Appendix for assembly instructions. The fully assembled gun is shown in the following figure:

Figure 4.16: Fully assembled ultrafast electron gun.

The gun is then installed by placing the front end through one of the vacuum chamber's walls and securing with 6 single claw clamps to make a vacuum tight seal.

Stellenbosch University http://scholar.sun.ac.za

Figure 4.17: Installation of the electron gun onto the vacuum chamber.

4.4 Magnetic lens

The magnetic lens is required to counteract the effect of the Coulomb repulsion experienced by the electrons. Each electron is negatively charged, repelling one another and causing the electron pulse the spread out radially (see figure 3.5). This effect increases drastically when increasing the electron number per pulse ($1000 - 30000$ e/pulse). The lens was designed[5] such that it would generate a

[5]Lens design, simulation and measurement thanks to Kerstin Haupt and Gunther Kassier

Stellenbosch University http://scholar.sun.ac.za

suitable magnetic field to force the electrons back together and therefore maintain spatial resolution of the measurements. It consists of a casing with many wires on the inside coiled around the central opening through which the electrons propagate. A current is passed through the wires to generate a suitable magnetic field in the central opening to counteract the Coulomb repulsion force.

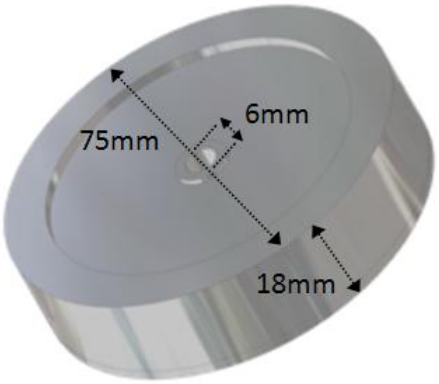

Figure 4.18: Magnetic lens design.

Such a lens produces donut-shaped magnetic field lines where the electrons propagate through the center of the 'donut'. The focusing of the electron pulse can be explained by considering the following figure of a two-dimensional slice through the center of the lens and the force experienced by a moving charged particle in the presence of a magnetic field, $\overrightarrow{\mathbf{F}} = q\overrightarrow{\mathbf{v}} \times \overrightarrow{\mathbf{B}}$ (where $q = -1.602 \times 10^{19}$ C is the charge of an electron in this case) [12].

Stellenbosch University http://scholar.sun.ac.za

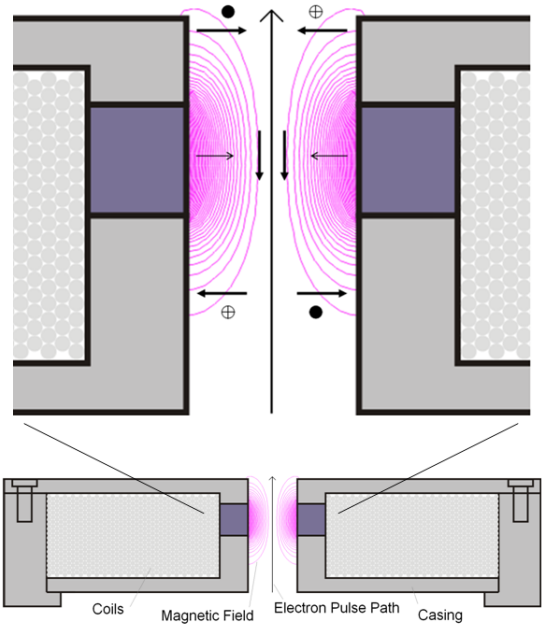

Figure 4.19: Cross-sectional view of lens's magnetic field - thick arrows indicate the magnetic field directions and the dots and crosses indicate the direction of the force on the electrons due to their velocity direction and the magnetic field direction.

The approximate direction of the magnetic field at different positions is indicated with thick arrows. The force an off-center electron experiences as it enters the lens is indicated by the dots and crosses (a dot indicating a force out of the page and a cross a force into the page). If a three dimensional magnetic field (donut-shaped) is considered this would cause the electron to start spiraling around the center of the lens as it propagates forward. This spiraling motion with the magnetic field direction as it is in the middle of the lens causes a inward force, towards the center, as can be seen by the thinner arrows. The force on the electron as it exits the lens is exactly opposite to when it enters the lens and therefore causes the electron to spiral in the opposite direction and therefore the spiraling motion is eliminated. All these mechanisms causes the focusing effect the magnetic lens has on the electron pulse

Simulations showed that about 400 Ampere-turn was needed to generate the required magnetic field strength to collimate a pulse of 10000 electrons with a kinetic energy of 30 keV.Itwas therefore decided to use roughly 600 windings (585 windings was the exact number) of wire that could carry a maximum current of 2 A. The total current could therefore be varied between 0 and 1200 A by varying the supplied current through the wire between 0 and 2 A. This is necessary because the magnetic field strength required is dependent on the number of electrons ($1000-30000$ e/pulse) and the kinetic energy (i.e. velocity) of the electrons.

Stellenbosch University http://scholar.sun.ac.za

The vacuum prevents the heat produced by the magnetic lens from dissipating into the surrounding atmosphere. If the current through the coils is set to 1 A (the normal operating current) the increase in temperature per hour of the lens is roughly 60° C ($\triangle T/s = \frac{P}{m \cdot c}$, with $P = RI^2 = 4$ W the power consumed by the lens, $m \approx 500$ g the mass of the copper wiring and stainless steel casing and $c \approx 0.5$ J/g·K the heat capacity of the copper/stainless steel mixture). The lens is therefore mounted in an encapsulating mount to conduct heat out of the lens and into the vacuum chamber floor. This prevents the temperature of the lens to increase to a temperature that would cause it to fail mechanically.

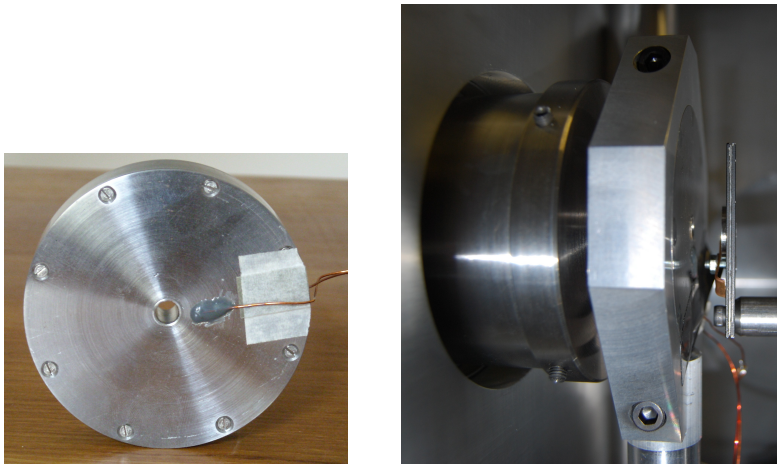

Figure 4.20: Final constructed magnetic lens and lens inside vacuum chamber mounted in an encapsulating mount. Electron gun visible on the left of the lens.

4.5 Vacuum chamber and vacuum pumps

The vacuum chamber was designed[6] to be as flexible as possible. It was therefore decided on a hexagonal shaped chamber (see fig 4.1), where the walls of the chamber comprise of six removable plates. Each plate can then be modified to the necessary requirements and moved to the necessary chamber face. A large perspex view port is situated on top of the chamber for observations.

[6]Chamber design thanks to supervisor, Prof. Heinrich Schwoerer

Stellenbosch University http://scholar.sun.ac.za

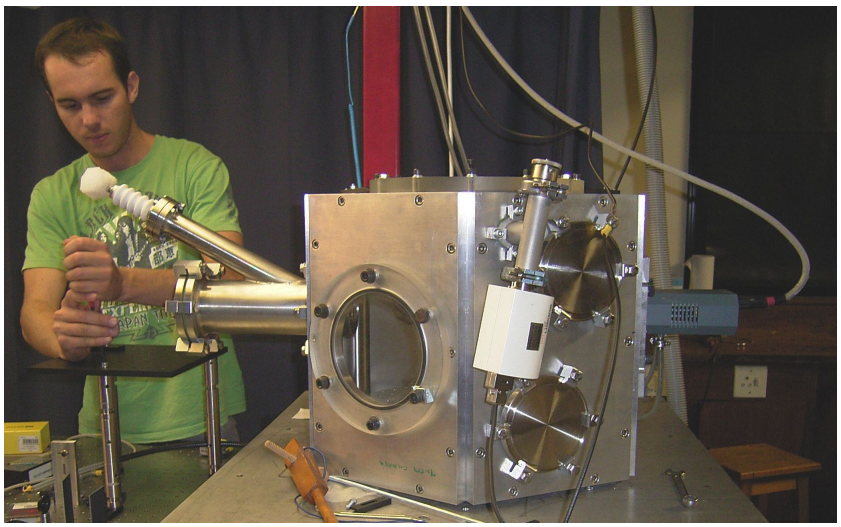

Figure 4.21: Vacuum Chamber - electron gun and myself visible on the left.

The chamber is placed on a separate table which allows the turbo pump to connect to the bottom of the chamber through a hole in the table's top. The rotary-vane pump is then connected to the turbo pump with a valve in between. The valve is closed before the rotary-vane pump is switched off to prevent any oil from the pump contaminating the chamber. The basic setup can be seen in the following figure:

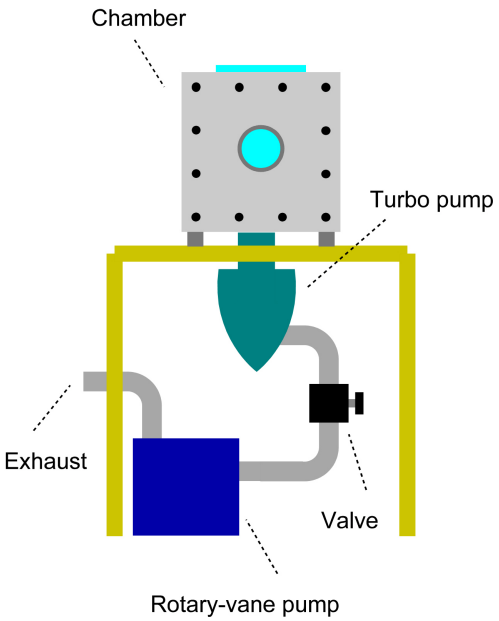

Figure 4.22: Vacuum system.

To perform electron diffraction experiments in transmission a vacuum of at

Stellenbosch University http://scholar.sun.ac.za

least 10^{-5} mbar is needed. For electron diffraction experiments in reflection 10^{-7} mbar is needed because surface contamination of the sample has a big effect on the produced diffraction pattern. The rotary-vane pump used is an *Adixen 2015SD* and has a pumping capacity of 15 m^3/h, which yields an ultimate pressure of roughly 10^{-2} mbar. The turbo pump used is a *Leybold TW70H* which has a pumping capacity of 60 l/s and can reach an ultimate pressure of 10^{-7} mbar. With the current setup a pressure of 10^{-2} mbar is reachable with the rotary-vane pump in roughly 30 min, but the turbo pump can already be switched on at a pressure of 10 mbar which is easily achieved after $1-2$ min. The ultimate pressure currently achievable with the turbo pump switched on is 9.2×10^{-6} mbar, which takes approximately 10 hours. However, a pressure of 10^{-4} mbar can been achieved, with a clean chamber, in roughly 15 min. This is sometimes sufficient to perform initial experiments. The pressure gauge employed is an *Adixen ACC 2009* and consists of a combination of a cold cathode ($10^{-8} - 10^{-3}$ mbar) and pirani gauge ($10^{-3} - 1000$ mbar) which gives us a total measuring range of $10^{-8} - 1000$ mbar.

The achievable vacuum at this stage is therefore sufficient for electron diffraction experiments in transmission but will need to be improved for experiments in reflection. The ultimate vacuum is however continuously being improved upon with tweaking to the vacuum system on a daily basis (as with any new system) and a vacuum of 10^{-7} mbar should be possible in the foreseeable future.

4.6 Electron detection

4.6.1 Phosphor screens

Phosphors screens use transition metal compounds or rare earth compounds that have the ability to 'glow' after exposure to energized particles like electrons or high energy photons. The phosphor molecules are excited by the energized particles into a metastable state and then radiatively decay (known as phosphorescence) after $1\ \mu s - 1$ s, depending on the type of phosphor used. The important parameters to consider when selecting an appropriate phosphor coating for particle detection are: 1) the sensitivity to the particle energy which one wishes to detect; 2) the wavelength of the emitted phosphorescence and 3) the decay time of the phosphorescence. These parameters are all dependent on the host material and activator. The most common host is zinc sulfide but many others also exist and the most common activators are typically copper or silver. Often the activators are mixed in the correct ratio to obtain the desired emitted wavelength and decay time. Emitted wavelengths range between 400 nm (blue) and 600 nm (orange) and decay times between a few micro-seconds and a few seconds. Phosphors are named by a 'P' followed by a number (e.g. P20, P43 and P47 etc.) [26].

To test the electron gun a phosphor screen from a discarded conventional electron microscope was used but a micro channel plate (see section 4.6.2) combined with a different phosphor screen was eventually used for the experiments because of a need for increased detection sensitivity. The type of phosphor used for the discarded screen is unknown but its emitted wavelength was green. The

Stellenbosch University http://scholar.sun.ac.za

phosphor used for the micro channel plate's phosphor screen is P43. P43 has a high quantum efficiency (60%) for 3 keV electrons (the acceleration voltage for the electrons in the micro channel plate is 3 kV, see figure 4.28). The wavelength of the emitted phosphorescence from P43 is 545 nm (green) and can therefore be detected by a conventional digital camera. The decay time of the phosphorescence is about 1 ms.

Below are the images taken upon testing the electron gun for the first time.

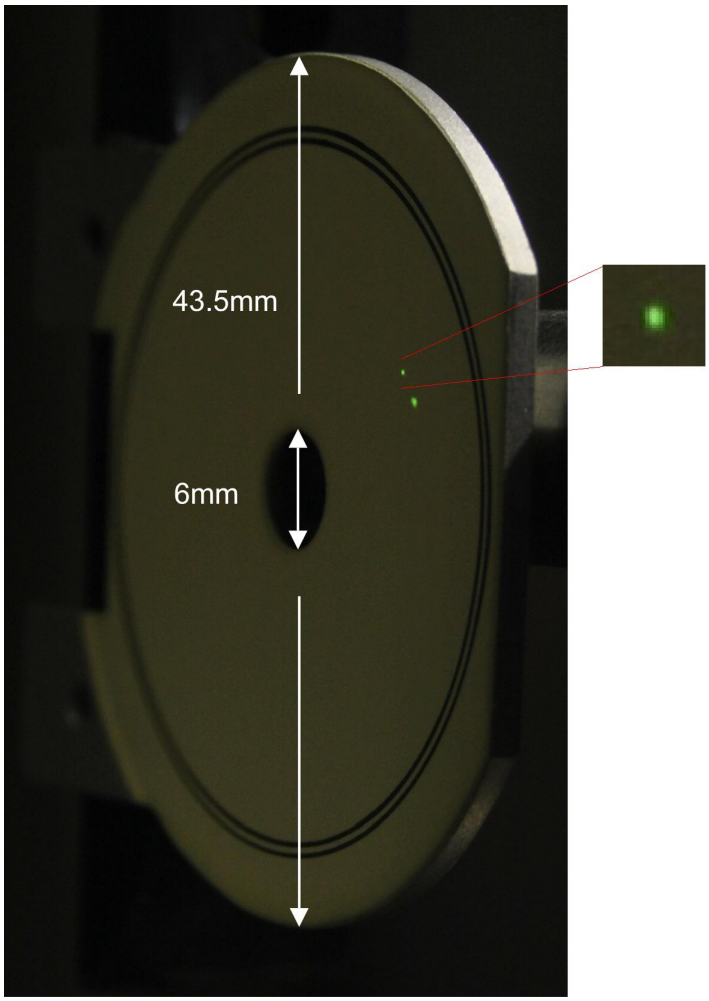

Figure 4.23: Electron detection with discarded electron microscope's phosphor screen.

The electron beam is the upper spot and the UV beam used for the electron generation (see section 3.3) is the lower spot. The reason why the UV spot is also visible is because the gold layer on the cathode (see fig 4.10 and 4.11) is only about 20 nm thick and is therefore semi-transparent to the UV beam. The UV photons also have a high enough energy to produce phosphorescence. The reason why the two spots do not fall on top of each other is because of slight

Stellenbosch University http://scholar.sun.ac.za

misalignment of the magnetic lens (see section 4.4). The UV photons are obviously not effected by the magnetic field of the magnetic lens but the electrons are focused by the lens and a slight misalignment also causes the electron beam to be slightly steered in a different direction.

These initial detections confirmed that the electron gun was functioning and it was then decided to place a test sample in the path of the electron beam to determine if an electron diffraction pattern was observable. The following image shows the diffraction pattern of a thin (50 nm) titanium foil. The second image was taken after optimizing the gun, re-aligning the magnetic lens and inserting a lens to focus the UV light onto the cathode (see fig 4.1, lens 3). This causes the generated electrons to be 'bunched' tighter and the effect is a more focused diffraction pattern[7]. Note how the UV beam is still visible (lower spot) even after passing through the titanium foil as well.

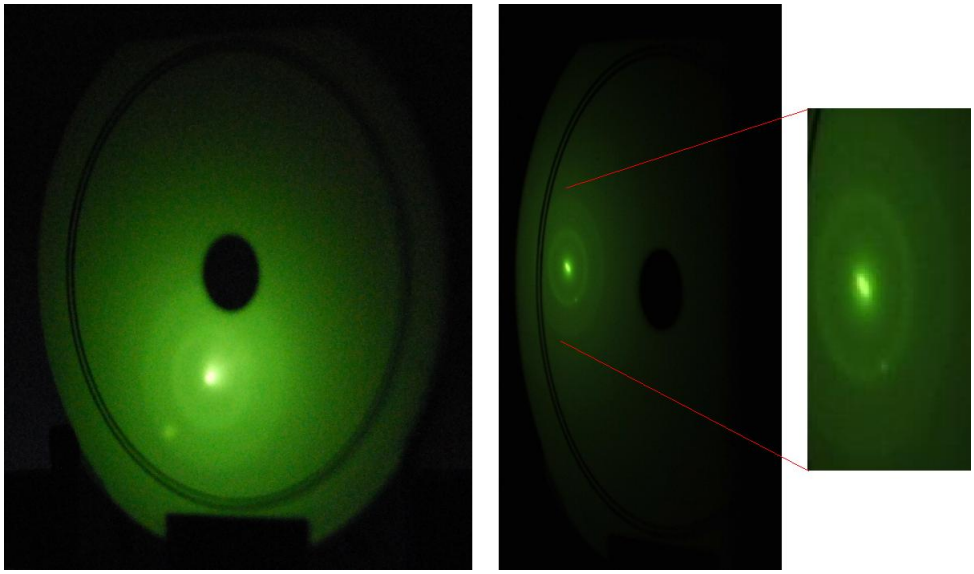

Figure 4.24: Electron diffraction pattern of 50nm titanium film.

4.6.2 Micro Channel Plates

In ultrafast electron diffraction experiments there is also always a compromise between electron number per pulse and pulse duration broadening (see section 3.4). In other words, the more electrons there are present in the pulse the brighter your diffraction pattern becomes but the also greater the Coulomb repulsion within the pulse becomes and therefore the quicker the pulse duration expands (which ruins the temporal resolution of the experiment). It is therefore desired to perform experiments with as few electrons in a pulse as possible and the requirement to detect as many of the electrons as possible becomes critical. Integrating over many shots of an electron pulse ($1000 - 30000$ e/pulse) can be done to overcome this problem but this is not always practical with all types of

[7] The screen was also placed closer to the sample which causes the diffraction rings to be smaller.

Stellenbosch University http://scholar.sun.ac.za

samples (for instance when the sample is destroyed after each shot).

Micro Channel Plates (MCP's) are devices that intensify the detection of a single particle or photon by means of secondary emission of electrons. The device is closely related to a Photo Multiplier Tube (PMT) and consists of an array of thousands of capillaries. These capillaries or channels are arranged in a honeycomb fashion and each one's inner wall is coated by a metal oxide, which has the ability to emit a few electrons when struck by a charged particle or a high energy photon. The channels are parallel to one another but angled at a small angle ($\sim 8°$) from the normal, which allows the incoming particles or photons to strike the inner wall.

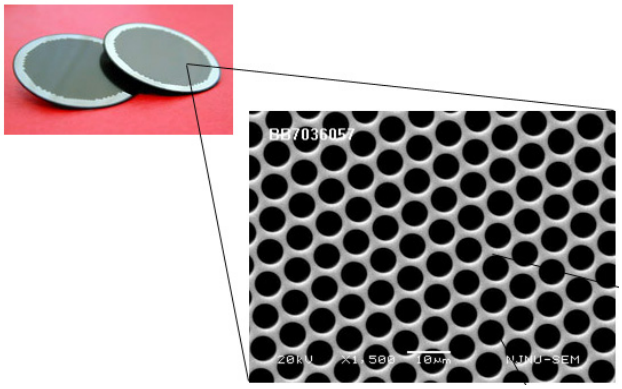

Figure 4.25: Microscopic view of the capillaries of a Micro Channel Plate, each capillary has a opening diameter of 12 μm with a center-to-center spacing of 15 μm.

The electrons that are emitted then strike the opposite side of the channel's wall and emit even more electrons. This then results in an snowball or avalanche effect producing millions of electrons from a single incoming particle or photon and amplifications of 1×10^4 - 1×10^8 are typical. The MCP consists of an active area and dead area, the active area being the entrance to the channels and the dead area being the space between. A particle that strikes the dead area will not be detected, but a ratio of the active area to dead area of 60% is common. The electrons that exit the rear of the MCP are then accelerated towards a conventional phosphor screen and the light emitted form the phosphor screen's phosphorescence can then be detected by a camera [24].

Stellenbosch University http://scholar.sun.ac.za

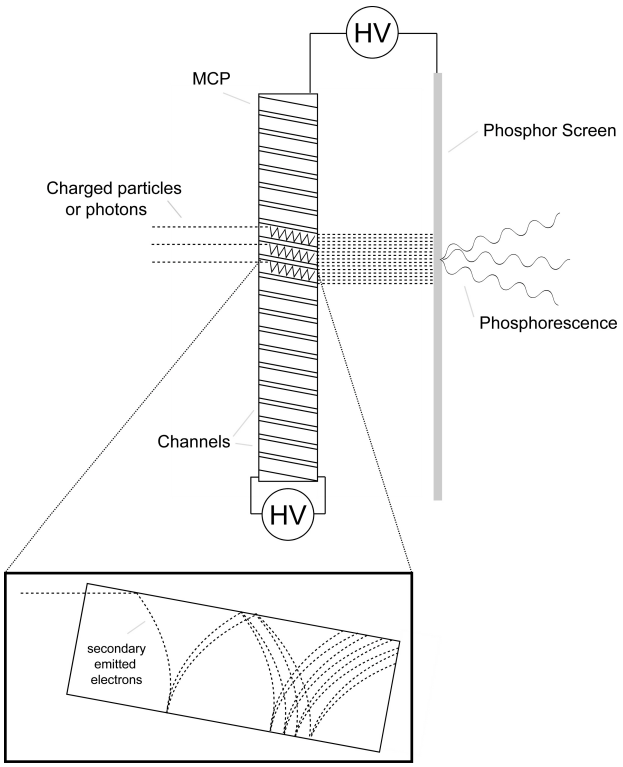

Figure 4.26: Micro Channel Plate Schematic - a single electron is amplified by an avalanche of secondary emitted electrons.

MCP's appear in several different configurations, but our research group decided on a Chevron MCP from *Tectra* (*MCP 050* with a P43 phosphor screen), with the light from the phosphor screen imaged in free-space onto a Charge-Coupled Device (CCD) chip by means of a lens (i.e. a conventional digital camera). The light from the phosphor screen is often coupled directly to the CCD chip by a tapered optical fibre bunch to reduce any loss and distortion of light. This obviously improves detection sensitivity but can drastically limit flexibility and increase cost. The Chevron configuration simply implies a double MCP, where the electrons that exit the first MCP are used as input to the second MCP. The channels of each plate are rotated 180° to one another, producing a chevron (v-like) shape.

Stellenbosch University http://scholar.sun.ac.za

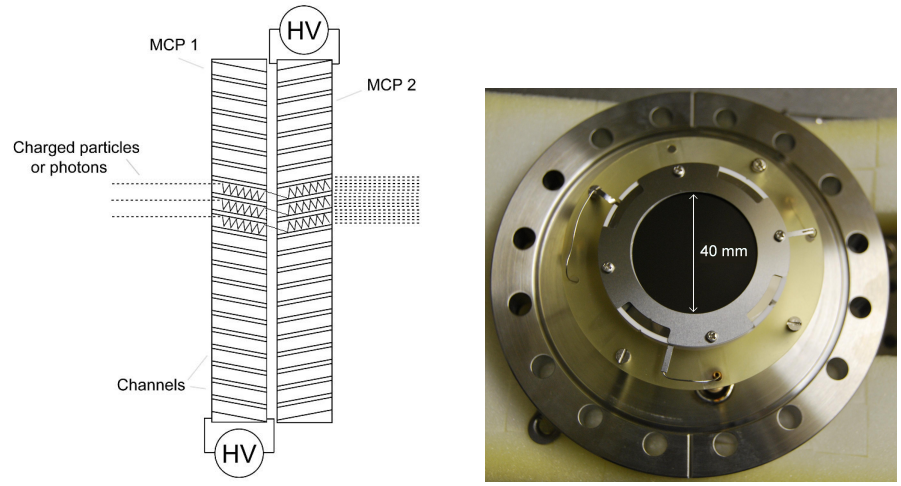

Figure 4.27: Chevron MCP configuration and detecting surface of MCP used in our setup.

Figure 4.28 shows the technical data and circuit [24] for the chevron MCP used in our setup. The circuit allows for a single power supply to be used for the three electron acceleration distances: 1) Front to rear of first MCP; 2) Front to rear of second MCP and 3) Rear of second MCP to phosphor screen. The maximum voltages that can be applied over the three distances are 1 kV, 1 kV and 4 kV respectively. The recommended voltages for the three distances are < 0.9 kV, < 0.9 kV and < 3.5 kV respectively. This gives a total voltage required to be roughly 5 kV. The voltage is supplied by a *Stanford PS350* power supply (maximum voltage = ± 5 kV, 5 mA), which can be computer controlled through a GPIB interface such that the voltage can slowly be ramped up in steps of 100 V to the desired voltage. This is recommended by the manufacturer to increase the operating life-time of the MCP (arcing inside the MCP can cause 'dead' capillaries).

Channel Length/Dia.	40:1
Outside diameter	50 mm±0.1mm
Active diameter	40 mm (min)
Thickness	0.5±0.05 mm
Center-to-center	15 µm
Pore diameter	12 µm
Bias angle	11°±1°
Open area ratio	60% min
Electrode resistance	250 MΩ (max)
Electrode penetration (of pore dia)	Input: 0.5±0.2 Output:0.5±0.2
Gain for single MCP	1×10^4 (min) @1000V
Gain for double MCP	5×10^6 (min) @2000V
Strip current	8-100µA @ 1000 V
Dark current	$<0.3\times10^{-12}$ A/cm² @ 1000V
Applied voltage	1000V (max)
Quality level	Detection grade/ Imaging grade

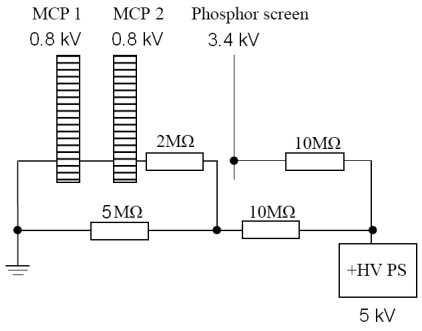

Figure 4.28: Technical data and circuit of MCP in our setup.

Stellenbosch University http://scholar.sun.ac.za

The camera used to capture the diffraction pattern is a *Nikon D60* which has a CCD chip with 10.2 million pixels. The chip is 15.8 mm×23.6 mm in dimensions and assuming a square pixel relates to a pixel size of 6 μm × 6 μm. The camera is equipped with a *Nikon AF-S DX* zoom lens, with a focal length range of $18 - 55$ mm and a minimum focal distance of 280 mm.

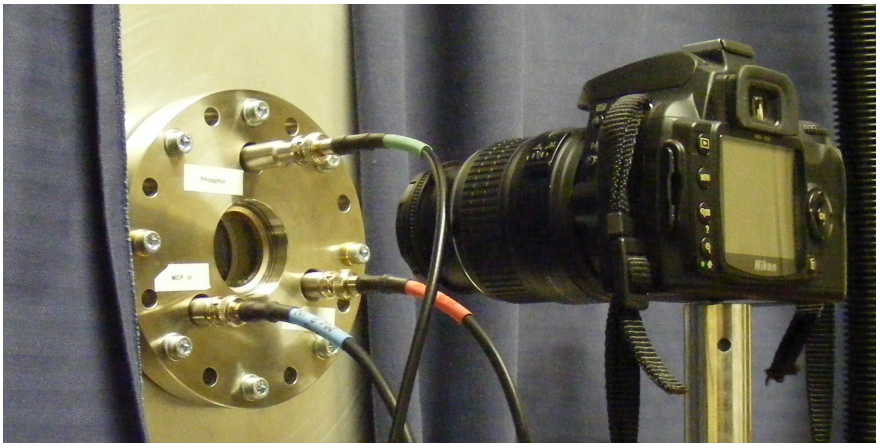

Figure 4.29: MCP-Camera setup in laboratory.

Each emitter on the phosphor screen radiates away from the screen in all directions (i.e. in 2π solid angle). The distance between the phosphor screen and camera is roughly 300 mm and the entrance of the lens has a diameter of 40 mm. The angle that is captured by the lens is therefore only about 8°, which is only 4.5% of the total radiated light. With an appropriate macro lens the captured radiated light could be increased by a factor of two but in this case the biggest limiting factor is the CCD chip size. A camera with a bigger CCD chip and an appropriate lens might need to be considered in the future.

In the following image we can see the improvement in resolution when the electron beam is detected as in figure 4.23, using the MCP. Note that the laser beam is not visible since the MCP has a very small efficiency ($< 1\%$) for UV light.

Stellenbosch University http://scholar.sun.ac.za

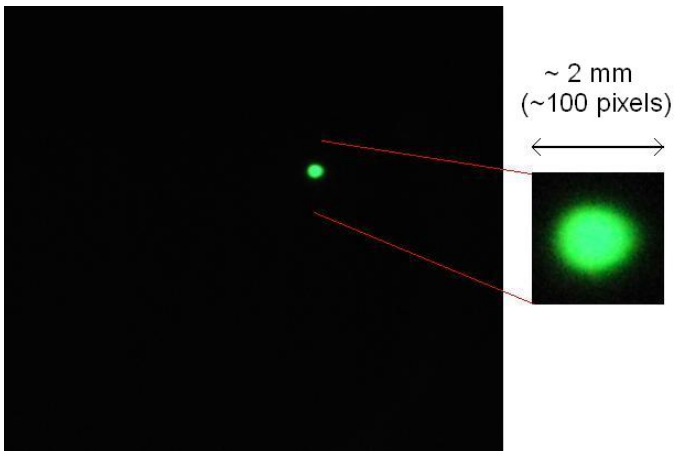

Figure 4.30: Electron detection with MCP.

This image shows the same diffraction pattern taken as in figure 4.24. Note how the increase in detection sensitivity clearly shows finer structures in the diffraction rings which were not visible in figure 4.24 (see section 6.5 for the analysis of this diffraction pattern).

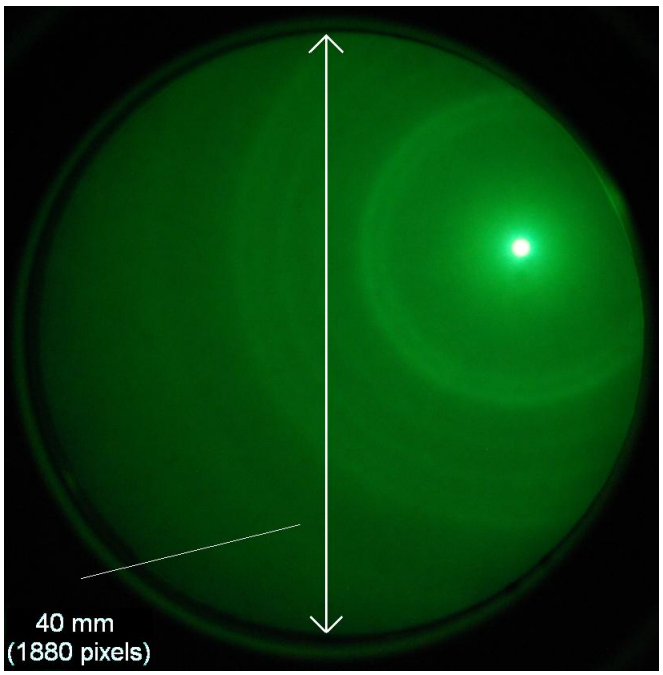

Figure 4.31: Electron diffraction pattern of 50nm titanium film detected with MCP.

From these images it can be calculated that the camera with the current lens has a resolution of about 20 μm slightly less than that of the MCP which is 15 μm (see figure 4.28).

Stellenbosch University http://scholar.sun.ac.za

5

Electron pulse characterization

Before time-resolved electron diffraction experiments can be performed the electron pulses have to be fully characterized. Information about the electron pulses that are important are: 1) The number of electrons per pulse because this effects propagation dynamics (see section 3.4); 2) The electron beam diameter at the sample because this effect the spatial resolution and 3) The electron pulse duration because this effects the temporal resolution of the 'pump-probe' experiment (see section 3.2).

5.1 Electron number per pulse

The photoelectric effect used to generate the electrons is a linear process (see section 3.3), therefore only one electron can be generated from a single photon, provided it has sufficient energy. This can be shown experimentally by recording the number of electrons per pulse generated, as a function of the laser's average power. This information is vital when performing diffraction experiments since the experimenter would often need to set the electron number per pulse, depending on the experimental requirements, since it was shown that the pulse propagation is strongly dependent on the number of electrons per pulse (see chapter 3.4). With this information the electron number per pulse can then easily be adjusted by adjusting the average power of the laser used to generate the electrons to the appropriate value. To measure the number of electrons per pulse a Faraday cup was used. The laser pulse energy can also be calculated if the frequency of the laser is known and from the pulse energy one can calculate the number of photons per pulse. Not every photon will produce an electron and the efficiency of the photon-to-electron conversion process can then also be calculated.

5.1.1 Experimental method and setup

The average power of the UV beam used for the electron generation was roughly adjusted by rotating a neutral density filter-wheel placed in the fundamental beam. The average power of the UV light was then finely adjusted by

Stellenbosch University http://scholar.sun.ac.za

rotating the wave-plate between the two non-linear crystals (see section 4.2 and figure 4.2). The number of photons in the UV pulse was calculated, $N_{\text{photons}} = \frac{E_{\text{pulse}}}{E_{\text{photon}}} = \frac{P_{\text{ave}}}{E_{\text{photon}} \times f}$ (with $E_{\text{photon}} = 7.66 \times 10^{-19}$ J the energy of a UV photon and $f = 1000$ Hz the frequency of the laser) [18].

The electron number per electron pulse generated was measured using a Faraday cup. This is an extremely simple device that can be used to 'count' electrons by measuring extremely small currents. The cup-shape is used to prevent any electrons from escaping if they happen to scatter of the surface of the metal, therefore not being detected. Electrons strike the inside wall of the cup and the metal from which it is constructed gains a small net charge. The metal can be discharged by grounding the cup, and the small current that is produced is measured [4]. Current is defined as the amount of charge that passes through a fixed point in the wire per second (i.e. $I = C/s$). The number of electrons that strike the cup per second is then $N_{(\text{electrons/sec})} = \frac{I}{e}$ (with $e = 1.60 \times 10^{-19}$ C the elementary charge of an electron). The number of electrons per pulse was then calculated by dividing by the electron pulse frequency (which is the same as the laser frequency), $N_{(\text{electrons/pulse})} = \frac{I}{e \times f}$.

If the electron number per pulse is assumed to be about 1000 e/pulse then this corresponds to a current of 1.6×10^{-13} A or 0.16 pA that needs to be measured. To measure such a small current is not impossible but also not trivial. It has to be mentioned that this is average current since the current is large during the duration of the electron pulse (which is a few hundred femtoseconds) but the multimeter will average over the entire individual pulse and over many pulses to measure a very small average current. It is therefore easier to measure voltage by introducing a large resistor into the circuit and measuring the relatively large voltage across the resistor. The current can then be calculated using Ohm's law, $I = \frac{V}{R}$. The electron number per pulse is then given by:

$$N_{(\text{electrons/pulse})} = \frac{V}{R \times e \times f} \tag{5.1}$$

Stellenbosch University http://scholar.sun.ac.za

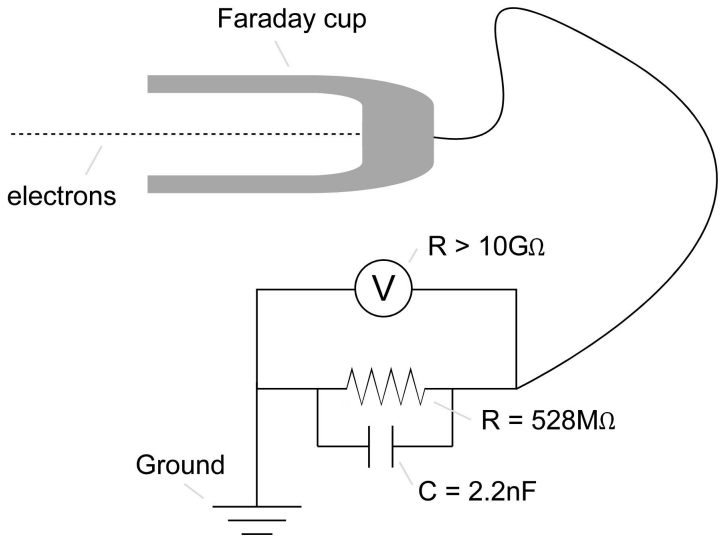

Figure 5.1: Schematic of Faraday cup circuit.

A resistor with a resistance of 528 MΩ was chosen, which makes the voltage measured across the resistor in the order of 0.1 mV if an electron beam with pulses of a 1000 e/pulse are captured by the Faraday cup (i.e. 0.16 pA of current passes through the resistor). This is realistic for the multimeter (*Agilent 34401A*) in our laboratory which has a measuring range of 1 μV − 1000 V and an accuracy of ±0.003 mV when measuring in the 0.1 mV range. A smoothing capacitor of 2.2 nF is also included in the circuit such that the time-constant of the RC circuit is roughly the same as the integration time of the multimeter, which was set at $\sim$ 1 s.

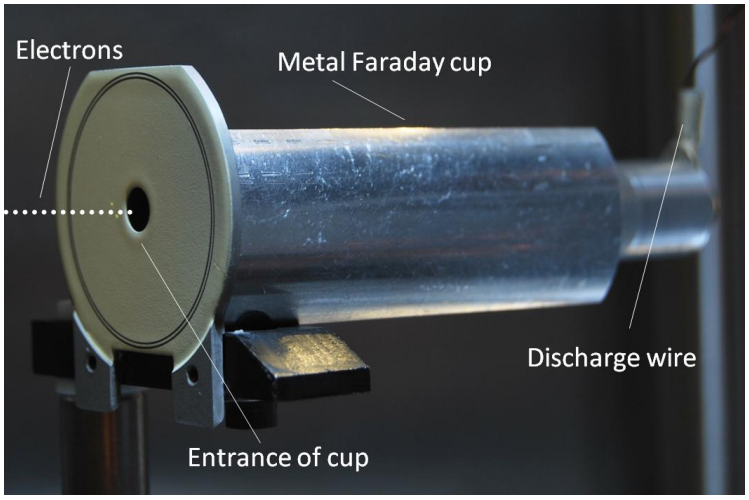

Figure 5.2: The Faraday cup in our setup, with a phosphor screen at the entrance that can be used for locating the electron beam.

Stellenbosch University http://scholar.sun.ac.za

5.1.2 Results

The measurements can be summarised in the following table.

UV power (μW)	Photon number per UV pulse	Voltage (mV)	Current (pA)	Electron number per electron pulse
9.70	1.27×10^{10}	0.19	0.36	2247
20.6	2.68×10^{10}	0.52	0.98	6117
31.0	4.05×10^{10}	0.83	1.57	9799
39.2	5.12×10^{10}	1.09	2.06	12858
50.0	6.52×10^{10}	1.45	2.75	17164
60.3	7.87×10^{10}	1.84	3.48	21720
73.9	9.65×10^{10}	2.43	4.60	28711

Table 5.1: Electron number per electron pulse as a function of input UV power.

The electron number per electron pulse as a function of input UV power can be plotted as well as the electron number per electron pulse as a function of photon number per UV pulse.

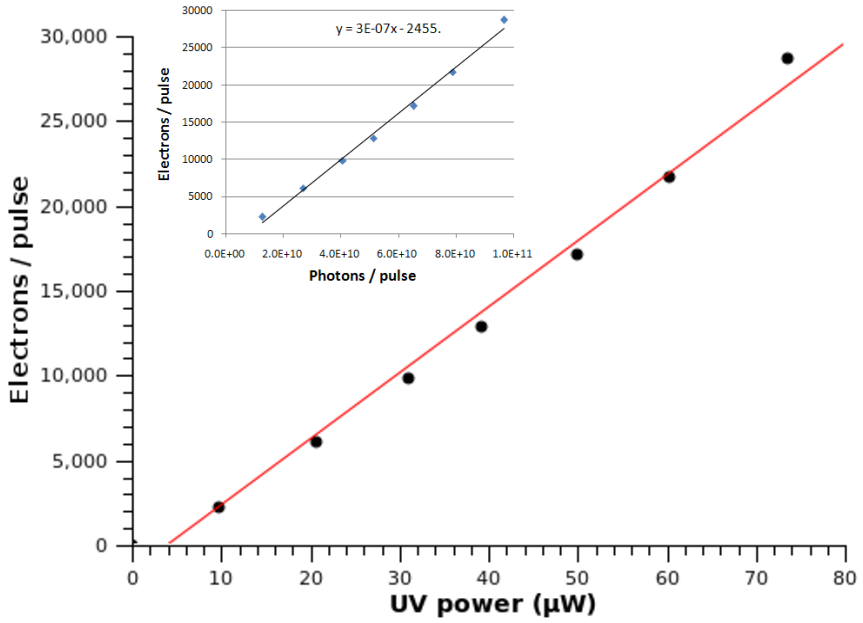

Figure 5.3: Electron number per pulse as a function of input UV laser power and as a function of UV photons per pulse.

The electron number per pulse can then easily be set by using the graph and adjusting the UV power to the corresponding value. The efficiency of the photon-to-electron conversion process can be calculated from the second graph's slope and is roughly 3×10^{-7}.

Stellenbosch University http://scholar.sun.ac.za

5.2 Electron beam diameter at the sample

In this experiment the diameter of the electron beam at the sample was determined. This is done by systematically sliding a sharp edge into the path of the beam and recording the electron number detected as a function of the edge's position. This can be done by either measuring the current with the Faraday cup and calculating the electron number (see section 5.1) or measuring the integrated intensity of the beam by integrating over all the pixels of the image recorded by the camera (see fig. 4.30). The latter method does not give the electron number but rather a relative measurement but this is sufficient for determining the beam diameter and this was the method chosen.

5.2.1 Experimental setup and principle

The following figure shows the experimental setup and the principle behind the experiment. Note that the electron beam is focused onto the detection screen and not onto the edge and that the edge is situated where the sample will be placed during diffraction experiments. This focusing regime will be the same when diffraction experiments are performed, where the beam is not focused on the sample but rather on the detection screen to produce a focused image of the diffraction pattern. We are interested in the beam diameter as it is at the sample. In the second figure one can see the sharp edge (stainless steel *Gillette* razor blade) glued onto the edge of the Faraday cup. The only reason for this was that the Faraday cup was positioned at the correct height and was already mounted on a motorized translation stage. The Faraday cup also has a phosphor screen attached to the front surface which aided in locating the electron beam before the edge could be slid into its path.

Stellenbosch University http://scholar.sun.ac.za

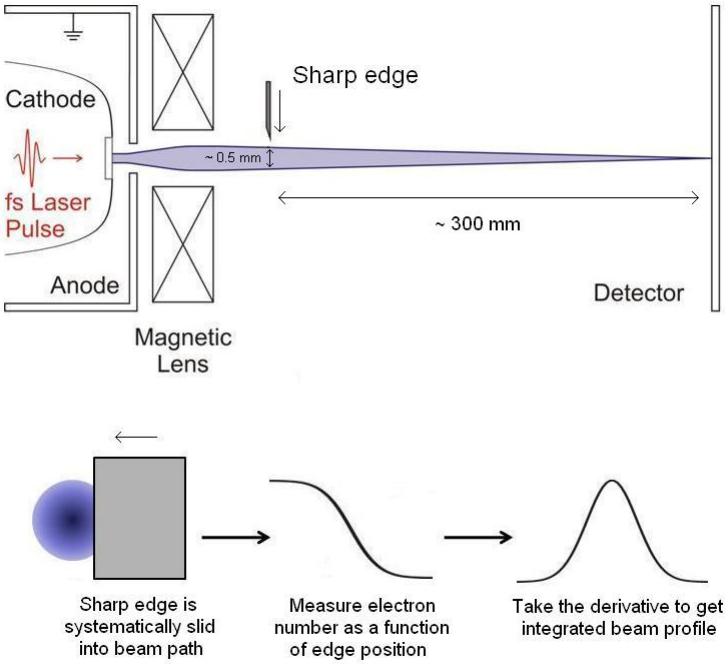

Figure 5.4: Experimental setup and principle of measuring electron beam diameter at the sample.

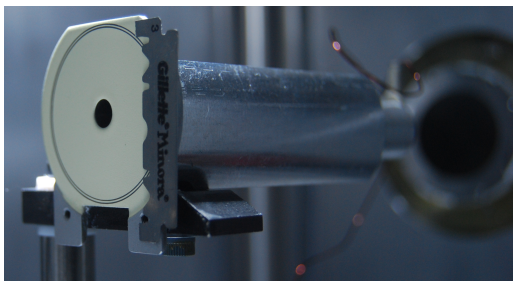

Figure 5.5: Sharp edge glued onto edge of Faraday cup - MCP in the background.

5.2.2 Results

The experiment was performed with maximum number of electrons per pulse achievable (30000 e/pulse) by our experimental setup in its current state. The beam diameter measured is therefore the maximum it could possibly be and will be smaller if pulses with fewer electrons are used, which will be the case when diffraction experiments are performed (see section 3.4). The figure shows some of the images captured the by the MCP and camera (see section 4.6.2) as the sharp edge was systematically moved into the beam path.

Stellenbosch University http://scholar.sun.ac.za

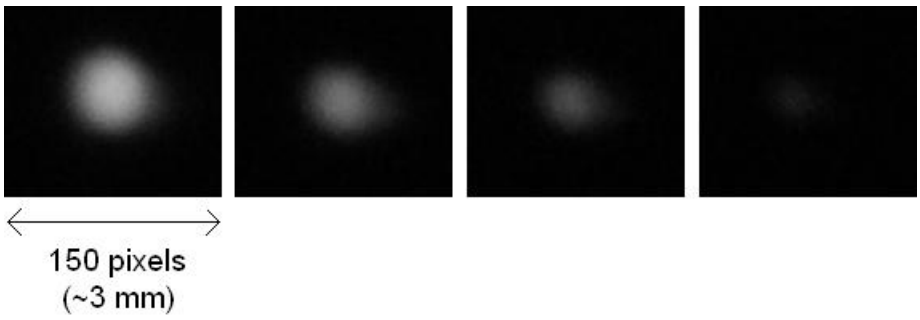

Figure 5.6: Fading of electron beam as edge is slid into beam's path.

The reason the sharp edge is not visible in the images is because the electron beam is focused on the MCP detector and not on the sharp edge. The following graph shows the normalized integrated intensity, calculated from the images collected. The fitted curve is also shown, which is an 'error function' and has a Gaussian curve as a derivative:

$$\mathrm{erf}(x) = \frac{2}{\sqrt{\pi}} \int_0^x \mathrm{e}^{-y^2} dy \tag{5.2}$$

with:

$$\frac{d}{dx}\mathrm{erf}(x) = -\frac{2}{\sqrt{\pi}}\mathrm{e}^{-x^2}. \tag{5.3}$$

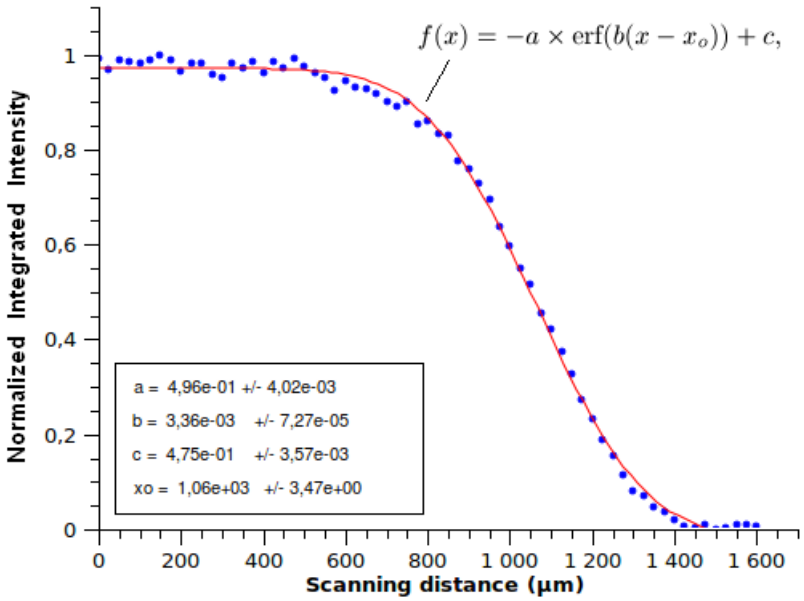

Figure 5.7: Electron beam profile measurement.

The derivative of the fitted function and therefore the integrated beam profile

Stellenbosch University http://scholar.sun.ac.za

can then be calculated using eq. 5.3.

$$g(x) = \frac{d}{dx}f(x) = -\frac{2ab}{\sqrt{\pi}}\mathrm{e}^{-b^2(x-x_o)^2} \tag{5.4}$$

Eq. 5.4 is plotted in the following figure and the Full-width-half-maximum (FWHM) shown. The FWHM of a Gaussian curve is given by: $\frac{2\sqrt{ln2}}{b}$ (see Appendix).

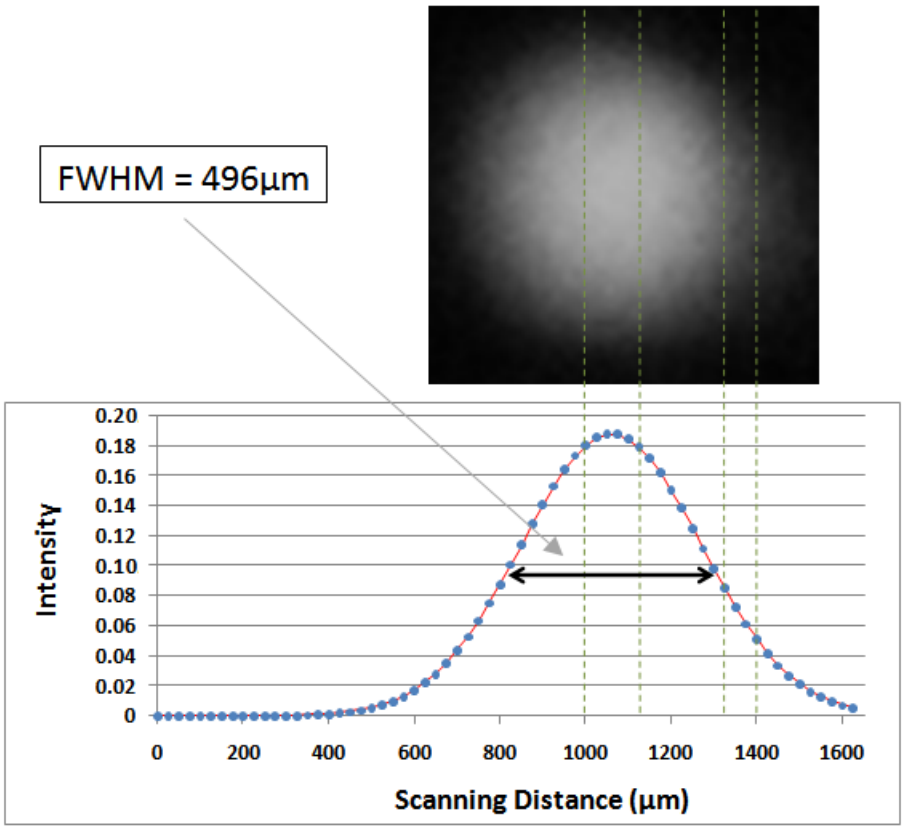

Figure 5.8: Integrated beam profile.

From the graph we can see that the electron beam diameter at the sample will be less than 500 μm since the electron number per pulse can be decreased or an aperture placed in the beam path. This is sufficient for electron diffraction experiments.

5.3 Proposed methods to measure pulse duration

Two experimental methods will be discussed from which the duration of an electron pulse can be determined. Both rely on the disturbance of the pulse path by means of an external force, that occurs on the same time scale as the pulse duration. By measuring the extent of the disturbance, which should be

Stellenbosch University http://scholar.sun.ac.za

dependent on the electron number, as a function of time, one can calculate the pulse duration.

5.3.1 Streak camera

This technique is implemented by applying a ramped electric field normal to the propagating direction of the electron pulse. If the ramping electric field is fast enough, the electrons at the front of the pulse will experience a different field strength to those at the back of the pulse. This causes different temporal parts of the pulse to be deflected at different trajectories, which produces a streak-like image of the of pulse on the detector. The pulse duration and the temporal profile of the pulse can then be determined by measuring the length and spatial profile of the streak pattern. By triggering a photo-conductive switch with a femtosecond optical pulse, it has been experimentally shown by Wang et al. [25] that a sufficient ramping electric field speed can be achieved to measure an electron pulse duration in the femtosecond time regime.

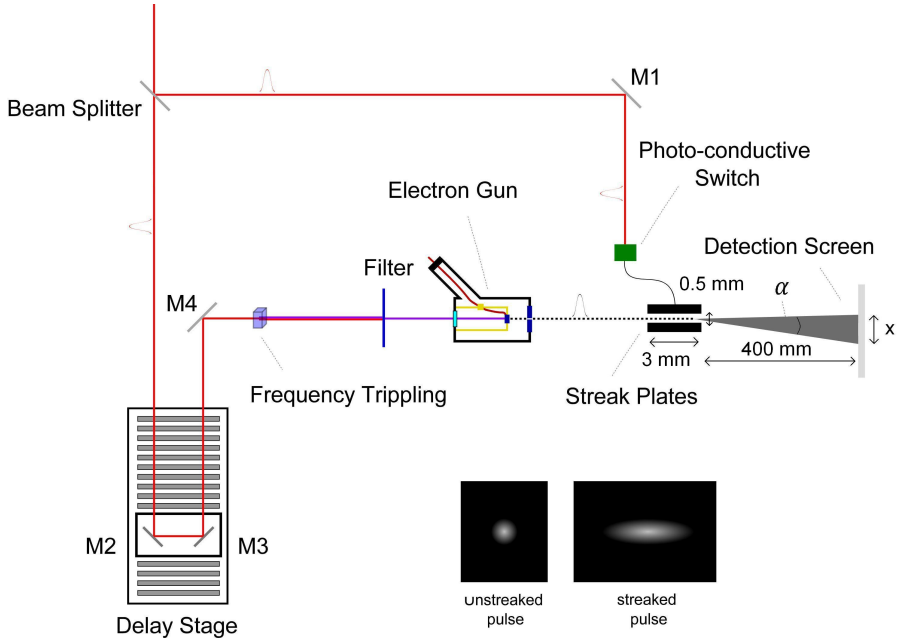

Figure 5.9: Proposed streak camera setup with expected unstreaked and streaked images.

To measure the true time duration of an electron pulse, the streaking force (i.e. the electric field) has to act on the electrons in the shortest propagating distance as possible, since the pulse duration increases as it propagates (see section 3.4). A distance of 3 mm would be short enough for pulse duration broadening to have little effect on the measurement but also big enough for realistic manufacturing of streaking plates of this size. For a propagating distance of 3 mm a 30 keV electron pulse would only be exposed to the streaking electric field for 30 ps. The changing electric field is an oscillating electric field produced by a simple LC circuit where the streaking plates are the capacitor and the first

Stellenbosch University http://scholar.sun.ac.za

slope of the oscillation is the streaking electric field. For a 30 ps exposure time to the first slope and assuming that the slope is roughly a third of the oscillation time, the oscillation would have to occur at 10 GHz ($\frac{1}{3} \times \frac{1}{10\ \mathrm{GHz}} \approx 33$ ps). This is possible with streaking plates (a capacitor) of 3 mm^2 and a separation distance of 0.5 mm where the frequency of the oscillation is, $\frac{1}{\tau} = \frac{1}{2\pi\sqrt{LC}}$ (the inherent inductance of the circuit is estimated to be a few nano-Henry and the capacitance of the streaking plates in a vacuum is, $C = \frac{\epsilon_0 \times Area}{d}$).

The remaining criteria would be to have a strong enough electric field for a streaking angle to be large enough to be be measured. For the images recorded with the MCP in our setup a resolution of 20 μm was obtainable (see figure 5.6). With the appropriate electron number and aperture it would be possible to have a unstreaked beam diameter on the MCP to be in the order of 200 μm. To have a measurable streaked image the streaking distance, x (see figure 5.9) would have to be $2-3$ times the size of the unstreaked beam diameter (i.e. $\sim$ 600 μm). With a distance of 400 mm between the MCP and the streaking plates that would yield a required streaking angle, $\alpha = 1$ mrad to obtain a measurable streaked image.

The streaking angle of an electron that experiences a force perpendicular to its propagating direction is given as, $\triangle\alpha = \frac{\triangle p_x}{p_z}$, where $\triangle p_x = \int_0^T F(t)dt$ is the change in momentum of the electron in the streaking direction and $p_z = m_e v_z$ the momentum of the electron in the propagating direction. The streaking angle can then be expressed as follow:

$$\triangle\alpha = \frac{\triangle E \times e \times t_p}{m_e v_z}, \tag{5.5}$$

with $t_p = 200$ fs the duration of the electron pulse. Therefore for a 30 keV electron pulse the required voltage across the streaking plates, for the electric field to produce a streaking angle of 1 mrad, is roughly 1.5 kV. This is realistic for a streaking plate separation distance of 0.5 mm.

The oscillating electric field can be triggered by a femtosecond optical pulse that activates a photo-conductive switch. The switch can for example consist of Ga-As which becomes conductive when illuminated by 850 nm light (it has a band gap of 1.4 eV). Our fundamental light of 775 nm would therefore be sufficient to use as a trigger for the electric field.

Considering all the issues discussed it should be possible to construct and incorporate a streak camera with the required specifications into our setup to measure electron pulses in the order of 200 fs. A prototype of a streak camera with the discussed specifications has already been designed and built by other members of my research group.

5.3.2 Laser ponderomotive scattering

Determining the pulse duration with a streak camera does have some limitations. The shorter the electron pulse becomes the the shorter the streak pattern becomes. If the length of the streak pattern becomes comparable to the unstreaked spot size then it becomes difficult to extract the pulse duration. This

Stellenbosch University http://scholar.sun.ac.za

can be remedied by increasing the ramped electric field, but this will also inevitably reach a physical limit. The distance to the streak pattern detector can also be increased but this as well has physical limitations due to the vacuum chamber size.

The alternative is to use the ponderomotive force that electrons will experience when interacting with a high intensity laser pulse. While the forces of a continuous plane wave on a charged particle cancel out over a cycle, this is not the case for an inhomogeneous field of a laser pulse. In this technique, parts of the electron pulse are sequentially scattered by overlapping it with the focus of a perpendicularly propagating, optical laser pulse. The extent of the overlapping can be controlled by inserting a delay line in the laser pulse's path and varying its path length. This technique has been successfully used in determining the pulse length of an electron pulse of a few hundred femtoseconds by Hebeisen et al. [11].

The disadvantage of this technique is that it requires a substantial peak intensity, in the order of 10^{17} W/cm^2. With current technology this is unreachable for most tabletop laser systems, including ours. It has however been suggested by Hebeisen et al. [11] that with an improved signal-to-noise ratio, a pulse energy of $\sim$ 1 mJ, which is obtainable from a conventional Ti:sapphire laser system, could be sufficient to perform an experiment like this.

In the final chapter, which follows hereafter, the theory behind how electron diffraction patterns are produced and how to retrieve information about the sample from the diffraction pattern will be discussed. This theory will be necessary to analyze diffraction patterns when time resolved electron diffraction experiments are performed.

Stellenbosch University http://scholar.sun.ac.za

6

Theory of electron diffraction

6.1 Electron diffraction patterns

In crystalline material, individual atoms, molecules or clusters of molecules, appear in periodic fashion within a two or three dimensional lattice like structure (see fig 6.1) This periodic structure, could serve as a type of 'diffraction grating' for x-rays or electrons.

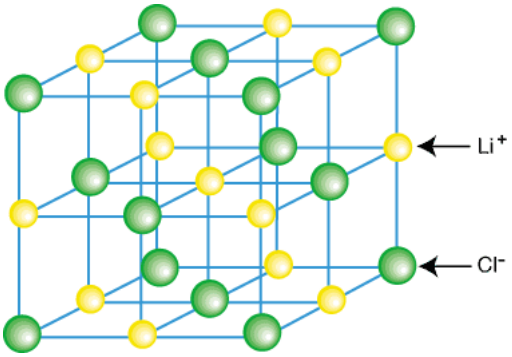

Figure 6.1: Crystal structure of LiCl.

The formation of the diffraction pattern can be understood by considering the scattering of two electrons from two parallel planes consisting of atoms in the crystal.

Stellenbosch University http://scholar.sun.ac.za

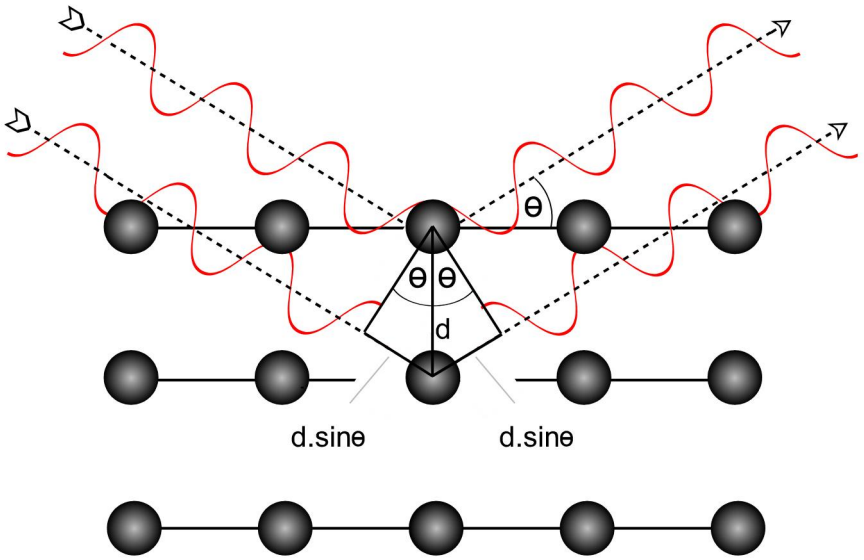

Figure 6.2: Bragg criterion.

In order for constructive interference to take place the angle should be such that the following criteria is met [5]:

$$2d\sin\theta = m\lambda, \qquad m = 1, 2, 3... \qquad , \tag{6.1}$$

where:

- d is the distance between the two planes
- λ is the de Broglie wavelength of the electrons
- m is the order of the interference fringe

This is known as the Bragg equation and can be used to calculate the plane-spacing or d-spacing of a crystal's diffracting planes. The Bragg equation is used to retrieve dimensional information from the crystal and how this is done will be discuss in more detail in section 6.3.

6.2 Types of patterns

Different types of diffraction patterns will occur depending on the type of crystal used. The two types of patterns are: single crystal and polycrystalline patterns [3].

Single crystal patterns occur when working with a crystalline specimen in which the periodic structure is uniform throughout the specimen as seen in the following figure.

Stellenbosch University http://scholar.sun.ac.za

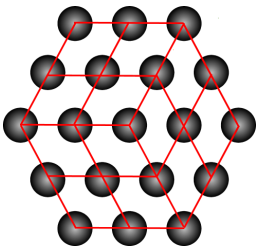

Figure 6.3: Uniform single crystal.

The shape of the diffraction pattern is dependent on the orientation of the crystal with respect to the electron beam.

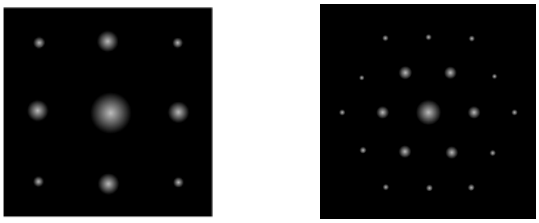

Figure 6.4: Example of a square and hexagonal, single crystal diffraction pattern.

Polycrystalline patterns occur when the crystalline specimen has a large number of discrete areas where the orientation of the atomic arrays differ.

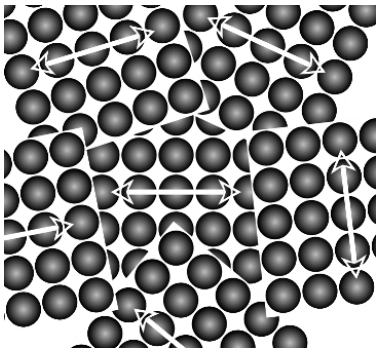

Figure 6.5: Polycrystalline structure.

This results in a ring-like diffraction pattern as seen in the left-hand side of fig 6.6 (the right-hand side is that of a single crystal), and can easily be understood when considering that the pattern is simply the superposition of many single crystal diffraction patterns, each rotated by a small amount. For instance, the same diffraction pattern can be obtained if a long exposure picture was taken while rotating a single crystal specimen at a specific orientation with respect to the electron beam.

Stellenbosch University http://scholar.sun.ac.za

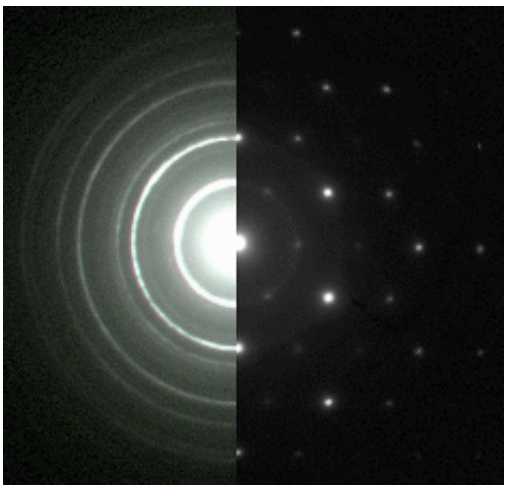

Figure 6.6: Polycrystalline diffraction vs. Single crystal diffraction.

6.3 Retrieving information and analysing electron diffraction patterns

In order to extract information and analyse a diffraction pattern, some fundamental information about crystals should first be gained.

6.3.1 Crystal systems

Each crystal lattice is defined by a unit-cell, which is the smallest 'building block' of the lattice. The unit-cell gives us the structural arrangement of the constituent atoms. If we consider the following two sketches then the seven crystal systems can be summarized in a table [3]:

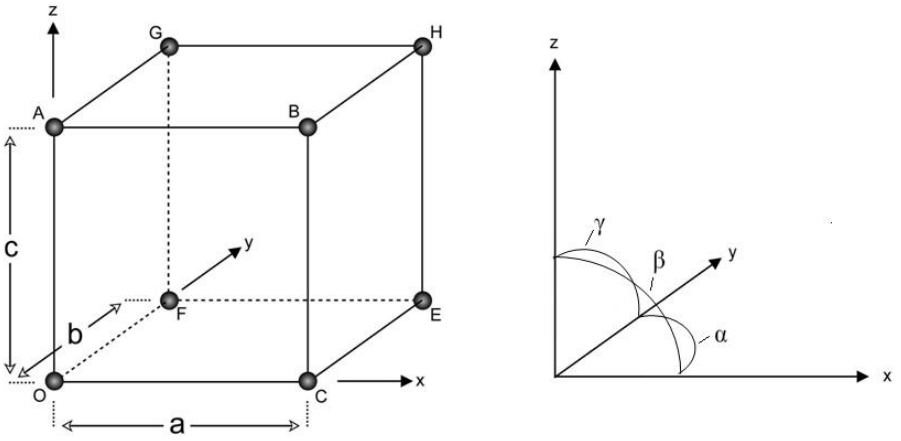

Figure 6.7: A crystal unit-cell.

Stellenbosch University http://scholar.sun.ac.za

Crystal System	Lattice spacing	Angle between axes
Cubic	$a = b = c$	$\alpha = \beta = \gamma = 90°$
Tetragonal	$a = b \neq c$	$\alpha = \beta = \gamma = 90°$
Orthorhombic	$a \neq b \neq c$	$\alpha = \beta = \gamma = 90°$
Rhombohedral	$a = b = c$	$\alpha = \beta = \gamma < 120° \neq 90°$
Hexagonal	$a = b \neq c$	$\alpha = \beta = 90°; \gamma = 120°$
Monoclinic	$a \neq b \neq c$	$\alpha = \gamma = 90° \neq \beta$
Triclinic	$a \neq b \neq c$	$\alpha \neq \beta \neq \gamma \neq 90°$

Table 6.1: The seven crystal systems.

6.3.2 Lattice planes - Miller indices

Previously it was mentioned that diffraction takes place because of scattering from parallel planes. Planes are labeled by a universally adopted system of indices, known as the Miller indices [3, 13]. The index takes the form of three numbers namely h , k and l and are defined as the reciprocals of the intercepts that the plane makes along the three axes x , y and z, in terms of the lattice parameters a , b and c. The Miller indices can then be defined as:

$$(hkl) = \left(\frac{a}{x_{int}} \frac{b}{y_{int}} \frac{c}{z_{int}} \right) \tag{6.2}$$

The idea is more easily understood by means of examples. Consider the following cubic lattice (i.e. $a = b = c$ and $\alpha = \beta = \gamma = 90°$):

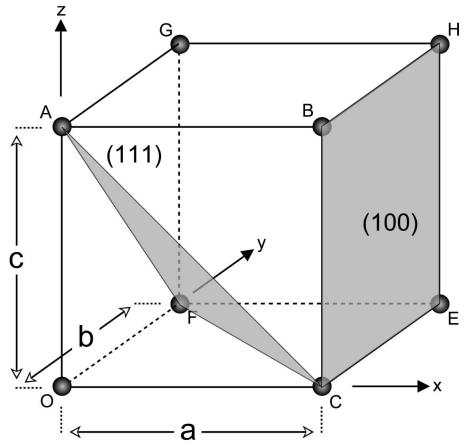

Figure 6.8: Cubic lattice showing the (111) and (100) planes.

The plane AFC intercepts the three major axes at $x = a$, $y = b$ and $z = b$, therefore the Miller indices are:

- $h = \frac{a}{x_{int}} = \frac{a}{a} = 1$
- $k = \frac{b}{y_{int}} = \frac{b}{b} = 1$
- $l = \frac{c}{z_{int}} = \frac{c}{c} = 1.$

Stellenbosch University http://scholar.sun.ac.za

The plane CBHE intercepts the three major axes at $x = a$, $y = \infty$ and $z = \infty$, therefore the Miller indices are:

- $h = \frac{a}{x_{int}} = \frac{a}{a} = 1$
- $k = \frac{b}{y_{int}} = \frac{b}{\infty} = 0$
- $l = \frac{c}{z_{int}} = \frac{c}{\infty} = 0.$

A more complex plane is shown in the following figure:

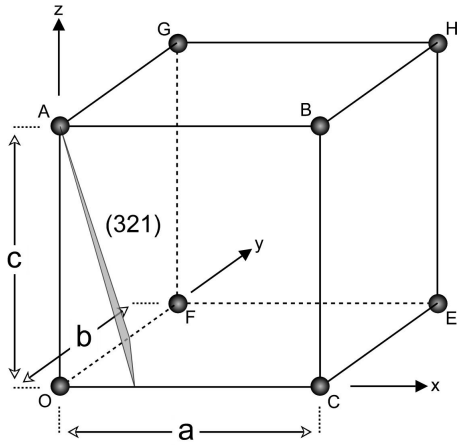

Figure 6.9: Cubic lattice showing the (321) plane.

The more complex plane intercepts the three major axes at $x = \frac{1}{3}a$, $y = \frac{1}{2}b$ and $z = c$, therefore the Miller indices are:

- $h = \frac{a}{x_{int}} = \frac{a}{\frac{1}{3}a} = 3$
- $k = \frac{b}{y_{int}} = \frac{b}{\frac{1}{2}b} = 2$
- $l = \frac{c}{z_{int}} = \frac{c}{c} = 1.$

The indices are always reduced to the lowest integer so the plane with intercepts $x = 2a$, $y = \frac{1}{2}b$ and $z = \infty$ will have the index (140) and not ($\frac{1}{2}$20). Planes that are exactly parallel to one another have the same indices. Therefore plane OAGF also has the Miller index of (100).

6.3.3 Determining the d-spacing

Now some information from the diffraction pattern can be retrieved. The following diffraction pattern is used as an example:

Stellenbosch University http://scholar.sun.ac.za

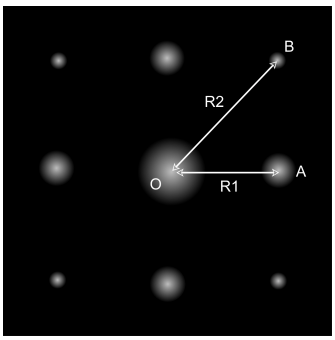

Figure 6.10: Example of a cubic crystal's diffraction pattern.

Previously it was shown that the d-spacing can be calculated by means of the Bragg equation (eq. 6.1). To calculate the d-spacing using the Bragg equation requires measuring the angle at which the diffraction spot in question occurs. It is however more sensible to derive a formula in terms of the distance between the center of the pattern and the diffraction spot (or ring), because this is what will be measured directly from the diffraction pattern (see fig 6.10). If the following geometry is taken into account, a formula can easily be derived.

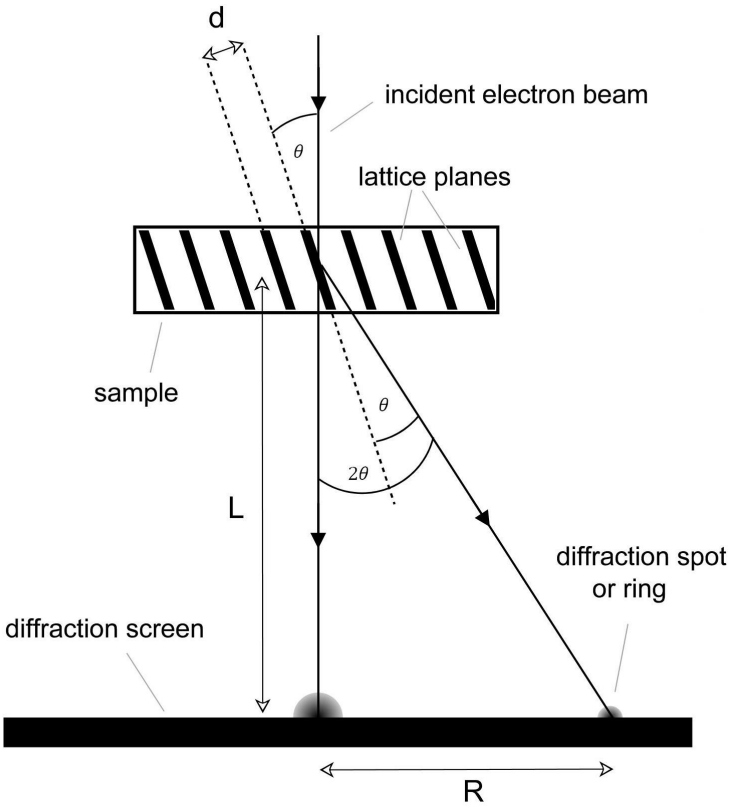

Figure 6.11: Diffraction geometry.

Stellenbosch University http://scholar.sun.ac.za

From fig 6.11 it should be clear that the following relationship holds, $\tan 2\theta = \frac{R}{L}$. If the Bragg equation[1] (eq. 6.1) is now substituted into this and it is accepted that for small angles of θ, $\tan 2\theta = 2\sin\theta$, then we are left with the very simple formula for d, the d-spacing:

$$d = \frac{\lambda L}{R}. \tag{6.3}$$

6.3.4 Indexing the diffraction spots or rings

The previous section showed how the d-spacing for each spot or ring in question can be calculated but which set of planes is being referred to for each individual spot or ring remains unknown. This can be done by using the equations shown in the Appendix. Indexing can be become rather tricky if the specimen is unknown so let the discussion be limited to a known specimen (i.e. the lattice parameters a , b and c as well as the lattice angles α , β and γ are known). To continue with an example, the following facts are considered:

- The crystal is cubic and the lattice parameter $a = 0.25$ nm.
- $R_1 = 4.8$ mm and $R_2 = 6.8$ mm.
- The electrons are accelerated to 40 keV, which implies they have a wavelength, $\lambda = 0.06$ Å(see figure 3.1).
- The distance from the sample to the observation screen is $L = 200$ mm.

Using eq. 6.3 the d for each spot is calculated:

$$d_1 = \frac{\lambda L}{R_1} = \frac{0.006 \text{ nm} \times 200 \text{ mm}}{4.8 \text{ mm}} = 0.25 \text{ nm}$$

$$d_2 = \frac{\lambda L}{R_2} = \frac{0.006 \text{ nm} \times 200 \text{ mm}}{6.8 \text{ mm}} = 0.176 \text{ nm}.$$

Using the relevant equation for a cubic lattice from the Appendix, the index for each spot can be calculated,

$$\frac{1}{d_1^2} = \frac{h_1^2 + k_1^2 + l_1^2}{a^2}$$

$$\Rightarrow h_1^2 + k_1^2 + l_1^2 = \frac{a^2}{d_1^2} = \frac{(0.25 \text{ nm})^2}{(0.25 \text{ nm})^2} = 1$$

$$\frac{1}{d_2^2} = \frac{h_2^2 + k_2^2 + l_2^2}{a^2}$$

$$\Rightarrow h_2^2 + k_2^2 + l_2^2 = \frac{a^2}{d_2^2} = \frac{(0.25 \text{ nm})^2}{(0.176 \text{ nm})^2} = 2$$

but h , k and l must be integers so

$$(h_1 k_1 l_1) = (100) \textit{ or } (010) \textit{ or } (001)$$

[1] To simplify matter in this regard, only the first order (i.e $m = 1$) is worked with and the other orders ignored.

Stellenbosch University http://scholar.sun.ac.za

and

$$(h_2k_2l_2) = (110)\ or\ (101)\ or\ (011).$$

The diffraction spots can now be indexed. First the center spot is assigned the index (000). Spot A can be assigned any one of the three possible indices but if it is assumed that one step to the right increases h by one and one step to the left decreases h by one, then it makes sense to assign spot A the index (100). Similarly, one step up increases k by one and one step down decreases k by one. If there is consistency with these rules then spot B is assigned the index (110). A negative index is indicated by a line above the integer. By following these rules the indices to all the spots, which can be seen in fig 6.12, can be assigned. The relevant planes for spot A and B are also shown in fig 6.13.

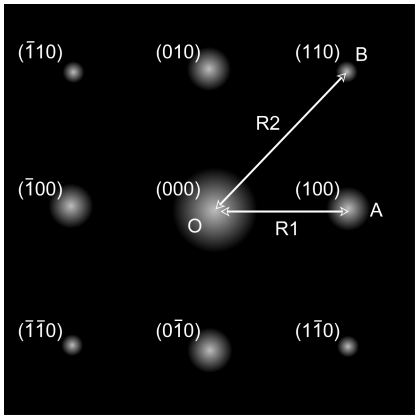

Figure 6.12: Indexing of diffraction spots.

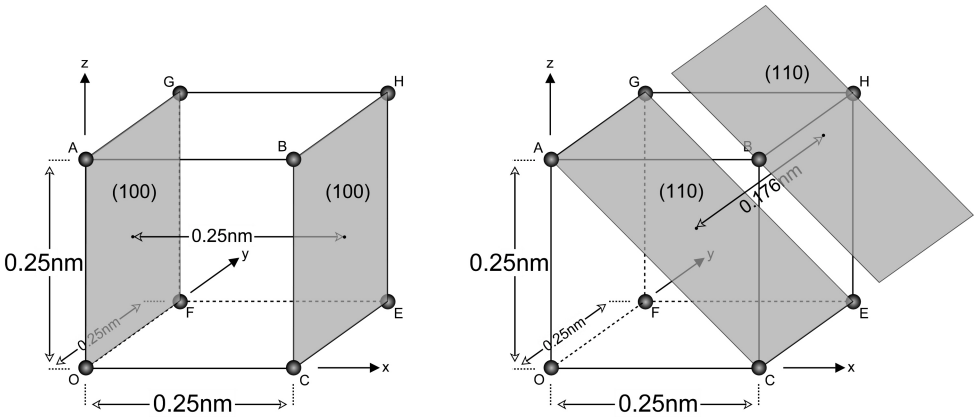

Figure 6.13: Relevant diffraction planes for spot A and B.

6.4 Reciprocal lattice and Ewald sphere

In the previous section, simple geometry was used to analyse and retrieve information from the electron diffraction patterns. This method is rather tedious

Stellenbosch University http://scholar.sun.ac.za

and becomes very difficult when analysing the diffraction patterns of more complex crystal types, like hexagonal or face-centered cubic crystals. There is another method that uses two geometrical concepts namely: the reciprocal lattice and the Ewald sphere. It is a less intuitive method at first, but very useful for analysing more complex diffraction patterns when mastered. The reciprocal lattice is a lattice construction where each lattice point represents a set of planes in the real crystalline lattice. The Ewald sphere is a geometrical construction that indicates which of the planes are reflecting (i.e. which planes produce diffraction spots and which planes do not) for a given incident wavelength and a given incident angle of the electron beam [1].

The exact construction of the reciprocal lattice is not discussed here but can be found in any solid state physics textbook. The important concepts of the reciprocal lattice is that each lattice point represents a set of lattice planes in the crystal (the lattice planes are discussed in detail in section 6.3.2) and that any point on the reciprocal lattice corresponds to a possible $\vec{\mathbf{g}}$ vector where the origin of $\vec{\mathbf{g}}$ lies at the origin of the reciprocal lattice and has a length $|\vec{\mathbf{g}}| = \frac{2\pi}{d_{hkl}}$, where d_{hkl} is the distance between the set of planes represented by the reciprocal lattice point. The following figure shows a sector of the reciprocal lattice for a face-centered cubic crystal [3].

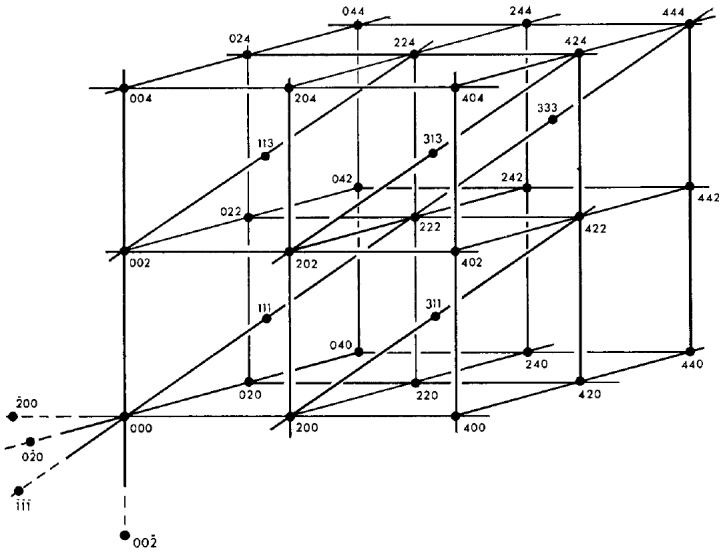

Figure 6.14: A sector of the reciprocal lattice of a face-centered cubic crystal.

The remainder of the reciprocal lattice can be added to represent the reverse side of the planes, where the indices include a bar over the Miller index to indicate that they are situated on the negative side of the reciprocal lattice's origin (see dotted lines in figure 6.14).

Using a construction known as the Ewald sphere the planes (represented by the reciprocal lattice points) which produce a diffraction spot, for a given wavelength, λ, and a given incident angle of the electron beam, can now be calculated.

Stellenbosch University http://scholar.sun.ac.za

Consider the following two dimensional slice of the reciprocal lattice in figure 6.14.

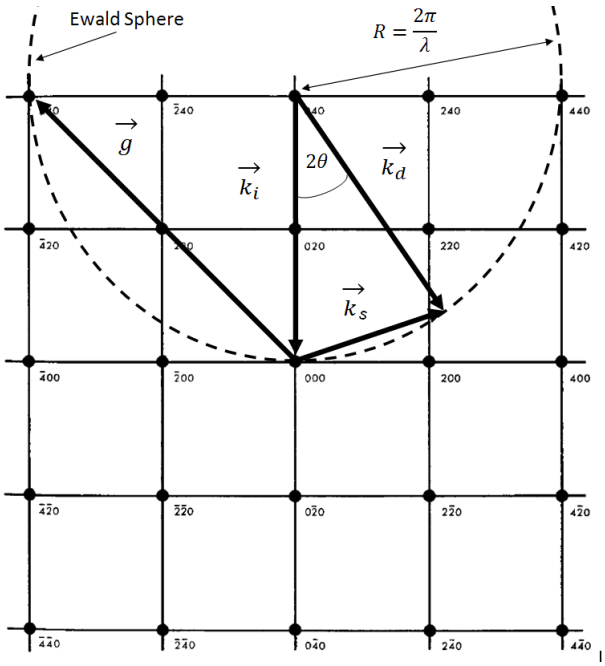

Figure 6.15: The Ewald sphere construction with an array of reciprocal lattice points.

The incident electron beam has a wave vector, $\vec{\mathbf{k}}_i$ that has a length $\frac{2\pi}{\lambda}$ and the diffracted beam has a wave vector, $\vec{\mathbf{k}}_d$. Elastic scattering occurs so that $|\vec{\mathbf{k}}_i| = |\vec{\mathbf{k}}_d|$ and the angle between them is 2θ (see figure 6.11). The scattering vector is, $\vec{\mathbf{k}}_s = \vec{\mathbf{k}}_d - \vec{\mathbf{k}}_i$ and from the figure the length can be calculated as $|\vec{\mathbf{k}}_s| = 2 \times |\vec{\mathbf{k}}_i| \times \sin\left(\frac{1}{2} \times 2\theta\right) = \frac{4\pi \sin\theta}{\lambda}$ (property of an isosceles triangle). For the Bragg equation to hold (i.e. $2d\sin\theta = \lambda$) it should be clear that $|\vec{\mathbf{k}}_s|$ has to equal $\frac{2\pi}{d_{hkl}}$, which is simply the value of $|\vec{\mathbf{g}}|$. The tip of $\vec{\mathbf{k}}_s$ always lies on the surface of the Ewald sphere and the tip of $\vec{\mathbf{g}}$ always lies on a reciprocal lattice point and that means that the Bragg equation only holds where the surface of the Ewald sphere intersects a reciprocal lattice point. Therefore only the sets of planes that are represented by these reciprocal lattice points will produce diffraction spots. The Ewald sphere is also of course a sphere in three dimensions and not only a circle as depicted in the figure above. Diffraction spots will therefore be produced by any sets of planes represented by the reciprocal lattice points that intercept the surface of this sphere.

If $\vec{\mathbf{k}}_i$ is now rotated but its tip still kept at the origin of the reciprocal lattice, a new Ewald sphere will be produced that intersects different reciprocal lattice points. In practice this is equivalent to rotating the sample with respect to the incident electron beam and doing so will make new diffraction spots appear at

Stellenbosch University http://scholar.sun.ac.za

different positions.

6.5 Indexing the diffraction pattern of a 50 nm titanium foil

The diffraction pattern recorded with our setup as seen in figure 4.31 can now be indexed using the theory that was discussed in the previous sections. The diffraction image was recorded using electrons with a kinetic energy of 37.2 keV (i.e. $\lambda = 0.063$ Å) and a distance between the MCP and the sample of $L = 350$ mm. The Bragg peaks are obtained experimentally by integrating along a fixed radius in the image of the recorded diffraction pattern. The radius of the ring is then converted to a diffracted angle, θ (see fig 6.11) and the intensity of the Bragg peaks can then plotted as a function of the length of the scattering vector $|\mathbf{k}_s| = \frac{4\pi \sin\theta}{\lambda}$ as per convention.

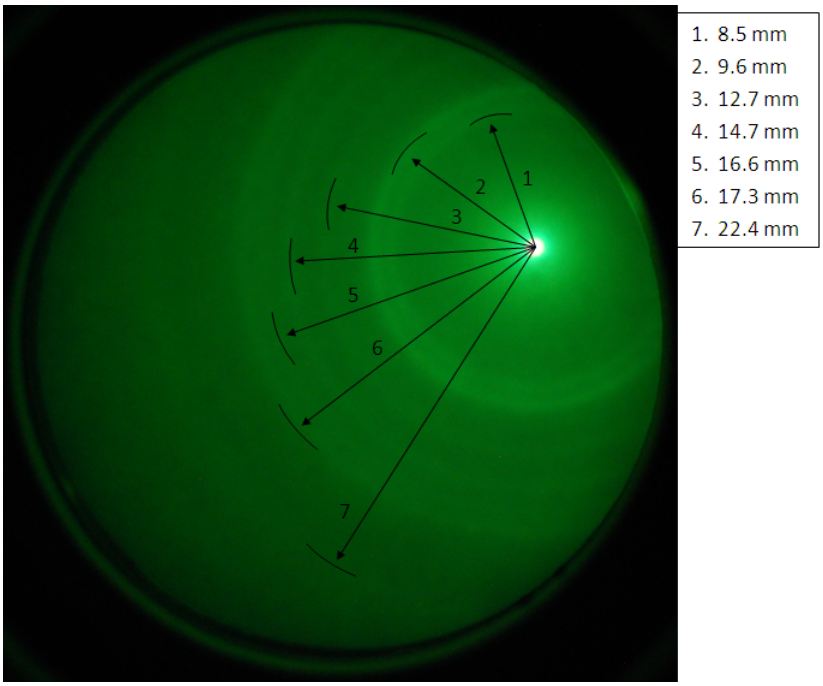

Figure 6.16: The diffraction pattern from a 50 nm titanium foil. Seven rings are visible with their measured radii.

Titanium has a hexagonal crystal system with lattice constants [16] $a = 2.995 \times 10^{-10}$ m and $c = 4.729 \times 10^{-10}$ m, so the theoretical d-spacing and therefore the associated diffracting angle using the Bragg equation ($2d\sin\theta = \lambda$) can be calculated where $\frac{1}{d_{hkl}^2} = \frac{4}{3}\left(\frac{h^2+hk+k^2}{a^2}\right) + \frac{l^2}{c^2}$ (see Appendix). The following figure shows the measured Bragg peaks with the planes that are possible theoretical matches to the peaks.

Stellenbosch University http://scholar.sun.ac.za

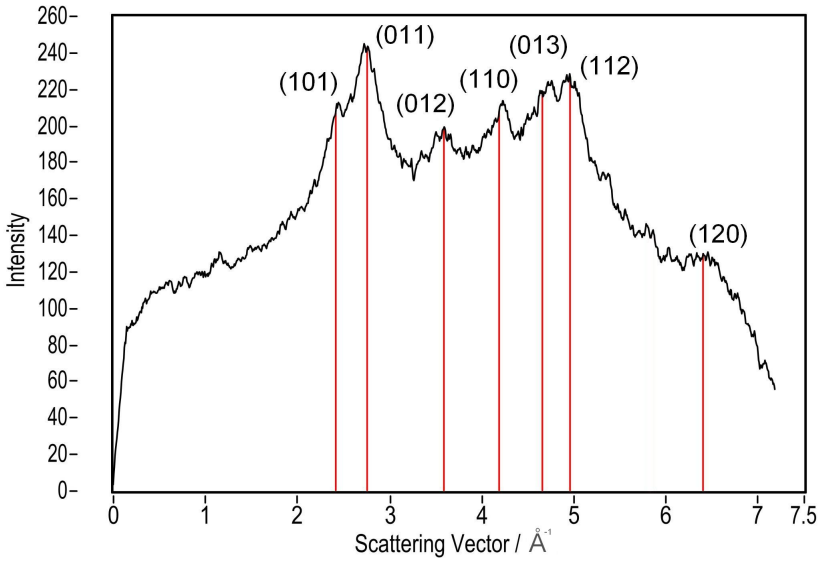

Figure 6.17: The Bragg peaks from the detected diffraction pattern of a 50 nm titanium foil. The vertical lines show planes that are theoretical matches for the peaks. The scattering vector is defined as $|\vec{\mathbf{k}}_s| = \frac{4\pi \sin\theta}{\lambda}$.

The above figure shows that there is an excellent correlation between the measured values and the theoretical values.

6.6 Analysing transforming diffraction patterns

In section 6.3 it was shown how information can be extracted from the diffraction pattern and how to interpret this information. The interpretation of the transformation of the diffraction pattern as the sample undergoes an ultrafast transformation now needs to be discussed. Typical observations that can be made are:

- The radius of the diffraction ring or the distance of the diffraction spot from the central spot could change.
- The cross-sectional intensity profile of the ring or spot could broaden or sharpen.
- The intensity of the ring or spot could decrease or increase.

Consider the diffraction pattern of the titanium foil from the previous section and the calculated peaks. These are known as Bragg peaks and each one represents a ring or spot on the diffraction pattern and therefore represents a set of planes inside the crystal (as discussed in section 6.3). The three typical observations that can be made are all due to changes in the orientation and spacing of the diffraction planes. The following figure summarizes the change that the planes experience and the result on the corresponding Bragg peak [19, 7].

Stellenbosch University http://scholar.sun.ac.za

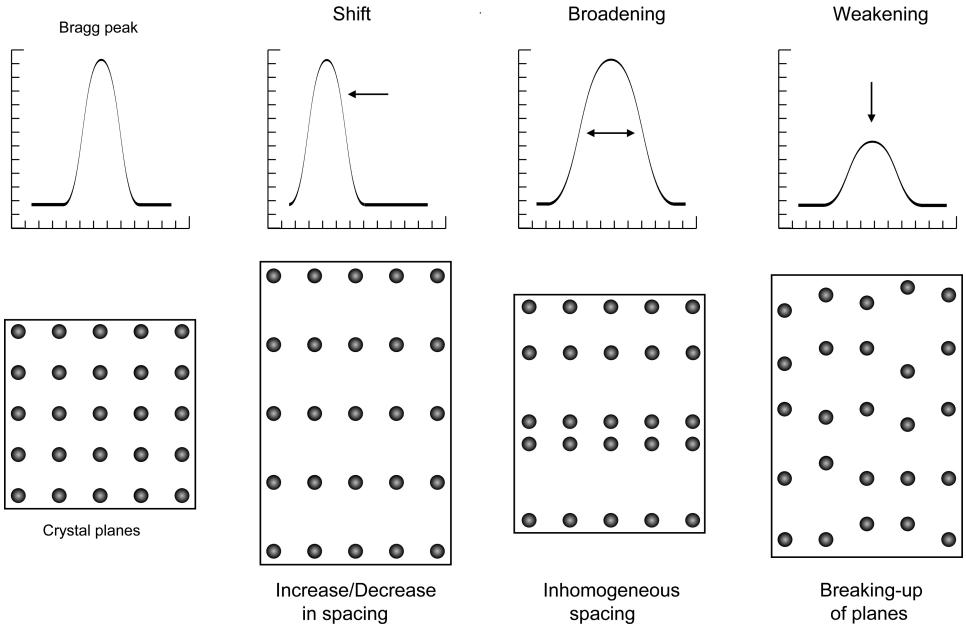

Figure 6.18: Bragg peak observations.

These observations have been used by Dwyer et al. [7] and Ligges et al. [17] to analyse the ultrafast heating of metals in the picosecond regime.

Stellenbosch University http://scholar.sun.ac.za

7

Summary and Outlook

A more intuitive technique for observing ultrafast dynamics of solids and molecules on the femtosecond time-scale was suggested, namely ultrafast electron diffraction which uses the observation of the ultrafast transformation of electron diffraction patterns. The role of the 'pump-probe' technique in observing these ultrafast photo-induced dynamics was discussed, as well as the reasoning behind the need for sub-picosecond electron pulses. The method of generating sub-picosecond electron pulses and the propagation dynamics of these pulses were also covered.

The design and construction of a working electron gun that can produce the sub-picosecond electron pulses required to perform ultrafast electron diffraction experiments was shown in detail. The constructed electron gun was able to produce electron pulses with electron numbers between $1000 - 30000$ e/pulse with a kinetic energy of up to 40 keV. A vacuum system, which houses the electron gun, that could reach an ultimate pressure of 9.2×10^{-6} mbar was also developed. Two electron characterization experiments were performed and the method and equipment needed for a third characterization experiment was discussed. The first characterization experiment showed the relationship between the electron number per electron pulse as a function of input UV power and the second characterization experiment determined the electron beam diameter at the sample. The third characterization experiment will be able to determine the electron pulse duration, which theoretically should be a few hundred femtoseconds.

The theory behind the source of the electron diffraction patterns and the different types of patterns were comprehensively discussed and it was further discussed how periodic spatial information, on the atomic scale, can be extracted from these patterns. Moreover, attention was given to how these diffraction patterns undergo an ultrafast transformation as the sample undergoes an ultrafast, photo-induced change and what information can be deduced from these transformations.

For future work one or both of the pulse duration experiments as suggested above need to be performed. The 'pump' beam for the 'pump-probe' setup should be included in the current setup. Initial experiments then need to be ex-

Stellenbosch University http://scholar.sun.ac.za

ecuted to test the system in its entirety. This may include the heating or melting of various thin metal foils and observing lattice structure changes in the picosecond regime. These experiments have been done before by other groups [7, 17] and the results can therefore be verified. Once these 'proof-of-principle' experiments have been performed, more intricate molecules that display photo-induced structural changes can be studied.

Stellenbosch University http://scholar.sun.ac.za

8

Appendix

Useful constants:

University Physics - Hugh D. Young [12]

$e = 1.602 \times 10^{-19}$ C
1 eV $= 1.602 \times 10^{-19}$ J
$m_e = 9.11 \times 10^{-31}$ kg
$h = 6.62 \times 10^{-34}$ J·s
$c = 3 \times 10^{8}$ m/s
$\varepsilon_0 = 8.85 \times 10^{-12}$ F/m

Stellenbosch University http://scholar.sun.ac.za

Assembly steps for electron gun:

1. Firstly the macor tube is secured to the rear, quartz windowed flange and the flange is then secured onto the gun shell by sliding the macor tube into the gun.

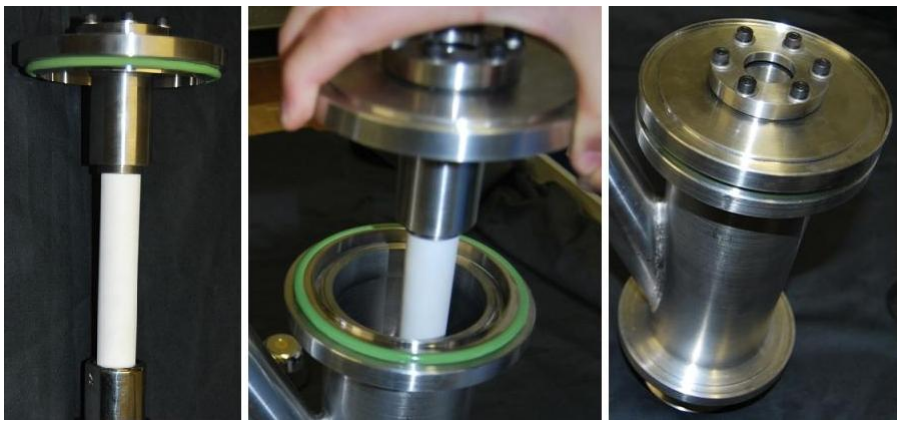

Figure 8.1: Step 1 - Attaching rear flange and macor tube.

2. The flange is then rotated until the high voltage rod's hole is aligned with the diagonal tube of the gun shell. The flange is then secured with clamps and the gun is turned around so that the Rogowski head can be screwed onto the other end of the macor tube.

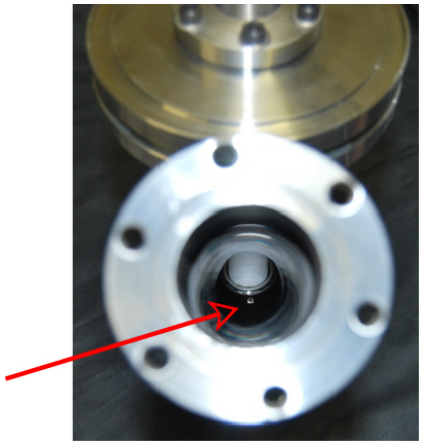

Figure 8.2: Step 2a - Aligning high voltage connection.

Stellenbosch University http://scholar.sun.ac.za

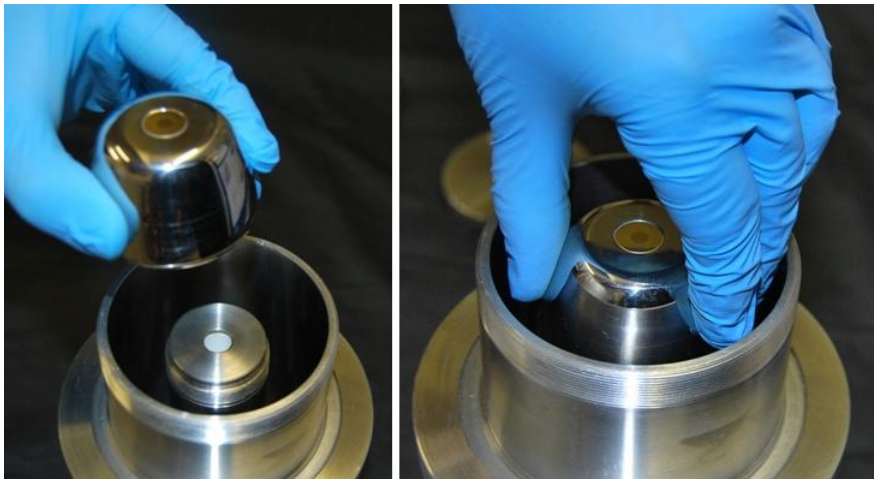

Figure 8.3: Step 2b - Securing the Rogowski head.

3. The high voltage rod can then be attached by screwing it into the previously aligned hole.

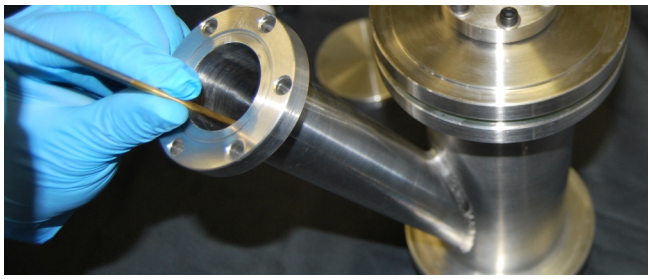

Figure 8.4: Step 3 - Attaching high voltage rod.

4. The high voltage feed through is then connected to the high voltage rod by sliding into the sleeve present on the other end. It is then secured onto the gun by 6 bolts.

Stellenbosch University http://scholar.sun.ac.za

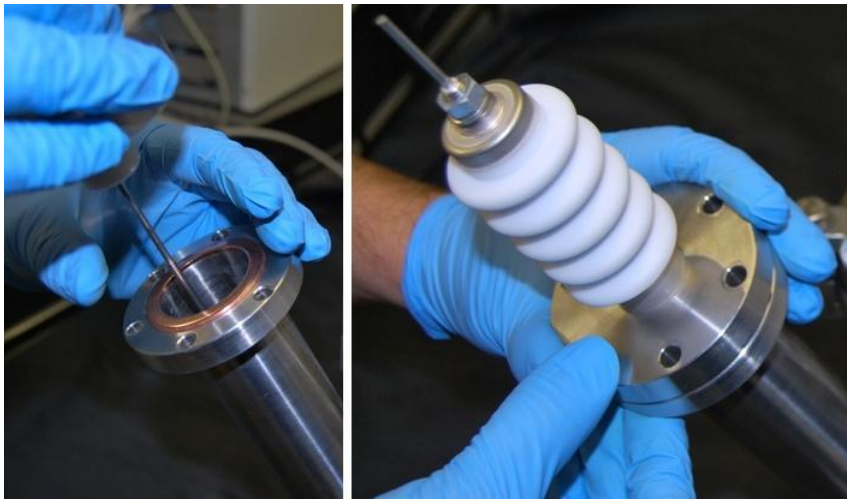

Figure 8.5: Step 4 - Attaching high voltage feed-through.

5. Finally the anode cap can be placed onto the gun and secured with the four 'grub' screws.

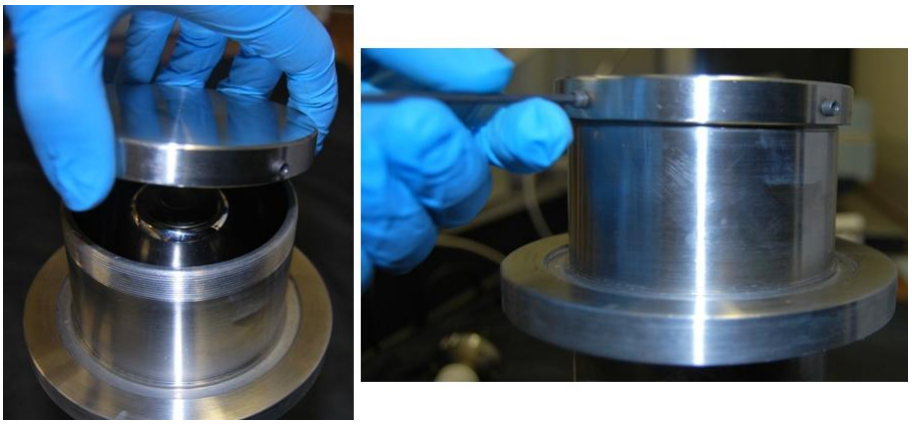

Figure 8.6: Step 5 - Securing the anode cap.

Stellenbosch University http://scholar.sun.ac.za

The d-spacing formula for the seven crystal systems:

Electron Diffraction and Optical Diffraction Techniques - Beeston [3]

Crystal System	Inter-planar spacing of the (hkl) plane
Cubic	$\frac{1}{d^2} = \frac{h^2+k^2+l^2}{a^2}$
Tetragonal	$\frac{1}{d^2} = \frac{h^2+k^2}{a^2} + \frac{l^2}{c^2}$
Orthorhombic	$\frac{1}{d^2} = \frac{h^2}{a^2} + \frac{k^2}{b^2} + \frac{l^2}{c^2}$
Hexagonal	$\frac{1}{d^2} = \frac{4}{3}\left(\frac{h^2+hk+k^2}{a^2}\right) + \frac{l^2}{c^2}$
Rhombohedral	see Appendix 2a (pg318) in [3]
Monoclinic	see Appendix 2a (pg318) in [3]
Triclinic	see Appendix 2a (pg318) in [3]

Stellenbosch University http://scholar.sun.ac.za

Calculating the FWHM of a Gaussian curve:

Consider the following Gaussian curve (see eq. 5.4):

$$g(x) = A\mathrm{e}^{-b^2(x-x_o)^2} \tag{8.1}$$

To simplify calculations, it is assumed the curve has no offset in the horizontal direction (i.e. $x_0 = 0$). This clearly has no effect on the FWHM of the curve. From the following it is clear that by solving for for x_- and x_+, the $FWHM = x_+ - x_-$.

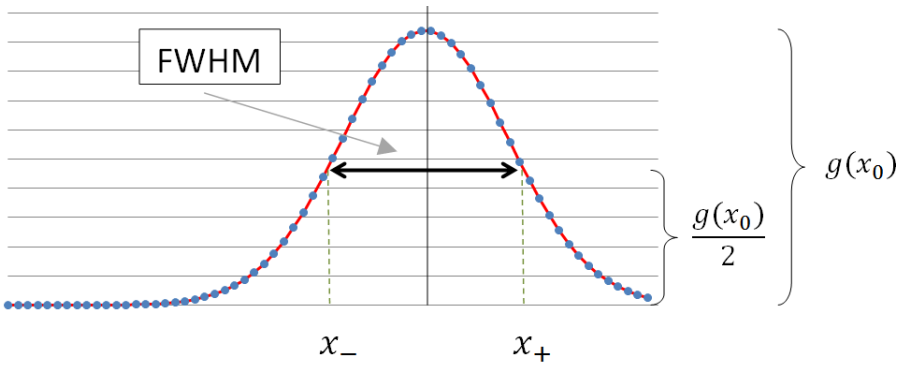

To obtain x_- and x_+ the following equation is solved:

$$\begin{aligned} g(x) &= \frac{g(x_0)}{2} \qquad (x_0 = 0) \\ Ae^{-b^2x^2} &= \frac{A}{2} \\ -b^2x^2 &= ln(\frac{1}{2}) \\ -b^2x^2 &= -ln(2) \\ x^2 &= \frac{ln(2)}{b^2} \\ x_\pm &= \pm\frac{\sqrt{ln(2)}}{b} \end{aligned}$$

The FWHM is then:

$$FWHM = \frac{2\sqrt{ln2}}{b}$$

Stellenbosch University http://scholar.sun.ac.za

Bibliography

[1] N.W. Ashcroft and N.D. Mermin. *Solid State Physics*. Brooks Cole, 1976.

[2] P. Baum, D. Yang, and A. Zewail. 4d visualization of transitional structures in phase transformations by electron diffraction. *Science*, 318, 2007.

[3] B. E. Beeston. *Electron Diffraction and Optical Diffraction Techniques*. Elsevier Science Ltd, 1994.

[4] K. L. Brown and G. W. Tautfest. Faraday-cup monitors for high-energy electron beams. *Review of Scientific Instruments*, 27, 1956.

[5] Raymond Chang. *Chemistry*. McGraw Hill, 2002.

[6] M. Chollet, L Guerin, N Uchida, S Fukaya, H Shimoda, T Ishikawa, K Matsuda, T Hasegawa, A Ota, H Yamochi, G Saito, R Tazaki, S Adachi, and S Koshihara. Gigantic photoresponse in 1/4-filled-band organic salt (edo-ttf)2pf6. *Science*, 307, 2005.

[7] JR Dwyer, CT Hebeisen, R Ernstorfer, M Harb, VB Deyirmenjian, RE Jordan, and RJD Miller. Femtosecond electron diffraction: 'making the molecular movie'. *Philosphical Transactions of the Royal Society A-Mathematical Physical and Engineering Sciences*, 364, 2006.

[8] D. E. Eastman. Photoelectric work functions of transition, rare-earth, and noble metals. *Phys. Rev. B*, 2, 1970.

[9] A.P. French and E.F. Taylor. *An Introduction to Quantum Physics*. CRC Press, 1979.

[10] Douglas C. Giancoli. *Physics*. Prentice Hall, 1997.

[11] CT Hebeisen, R Ernstorfer, M Harb, T Dartigalongue, RE Jordan, and RJD Miller. Femtosecond electron pulse characterization using laser ponderomotive scattering. *Optics Letters*, 31, 2006.

[12] Roger A. Freedman Hugh D. Young. *University Physics*. Addison Wesley, 2003.

[13] Ayahiko Ichimiya and Philip Cohen. *Reflection High Energy Electron Diffraction*. Cambridge University Press, 2004.

Stellenbosch University http://scholar.sun.ac.za

[14] A. Janzen, B. Krenzer, O. Heinz, P. Zhou, D. Thien, A. Hanisch, F.-J. Meyer zu Heringdorf, D. von der Linde, and M. Horn von Hoegen. A pulsed electron gun for ultrafast electron diffraction at surfaces. *Review of Scientific Instruments*, 78(1), 2007.

[15] G. H. Kassier, K. Haupt, N. Erasmus, E. G. Rohwer, and H. Schwoerer. Achromatic reflectron compressor design for bright pulses in femtosecond electron diffraction. *Journal of Applied Physics*, 105, 2009.

[16] David R. Lide, editor. *Handbook of Chemistry and Physics*. CRC Press, 2008.

[17] M. Ligges, I. Rajkovic, P. Zhou, O. Posth, C. Hassel, G. Dumpich, and D. von der Linde. Observation of ultrafast lattice heating using time resolved electron diffraction. *Applied Physics Letters*, 94(10), 2009.

[18] Peter Milonni and Joseph Eberly. *Lasers*. John Wiley & Sons, 1988.

[19] Hyuk Park. *The Development of Femtosecond Electron Diffraction for Direct Measurement of Ultrafast Atomic Motion*. PhD thesis, Florida State University, College of Arts and Sciences, 2006.

[20] C Rischel and A Rousse. Femtosecond time-resolved x-ray diffraction from laser-heated organic films. *Nature*, 390, 1997.

[21] BJ. Siwick, JR. Dwyer, RE. Jordan, and RJD Miller. Ultrafast electron optics: Propagation dynamics of femtosecond electron packets. *Journal of Applied Physics*, 92, 2002.

[22] BJ. Siwick, JR. Dwyer, RE. Jordan, and RJD. Miller. An atomic-level view of melting using femtosecond electron diffraction. *Science*, 302, 2003. ISSN 0036-8075.

[23] BJ. Siwick, JR. Dwyer, RE. Jordan, and RJD. Miller. Femtosecond electron diffraction studies of strongly driven structural phase transitions. *Chemical Physics*, 299, 2004.

[24] *MCP Data Sheet and Set Up Manual*. Tectra Physikalische Instrumente.

[25] X. Wang, S. Nie, H. Park, J. Li, R. Clinite, R. Li, X. Wang, and J. Cao. Measurement of femtosecond electron pulse length and the temporal broadening due to space charge. *Review of Scientific Instruments*, 80, 2009.

[26] William M. Yen, Shigeo Shionoya, and Hajime Yamamoto. *Phosphor Handbook*. CRC Press, 2006.